Reports on Progress in Physics

REVIEW

Interference traps waves in an open system: bound states in the continuum

To cite this article: Almas F Sadreev 2021 *Rep. Prog. Phys.* **84** 055901

IOP Publishing Reports on Progress in Physics
Rep. Prog. Phys. **84** (2021) 055901 (33pp) https://doi.org/10.1088/1361-6633/abefb9

Review

Interference traps waves in an open system: bound states in the continuum

Almas F Sadreev*

Kirensky Institute of Physics, Federal Research Center KSC SB RAS, 660036 Krasnoyarsk, Russia

E-mail: almas@tnp.krasn.ru

Received 28 September 2020, revised 29 January 2021
Accepted for publication 17 March 2021
Published 27 April 2021

Abstract

I review the four mechanisms of bound states in the continuum (BICs) in the application of microwave and acoustic cavities open to directional waveguides. The most simple are symmetry-protected BICs, which are localized inside the cavity because of the orthogonality of the eigenmodes to the propagating modes of waveguides. However, the most general and interesting is the Friedrich–Wintgen mechanism, when the BICs are the result of the fully destructive interference of outgoing resonant modes. The third type of BICs, Fabry–Perot BICs, occurs in a double resonator system when each resonator can serve as an ideal mirror. Finally, the accidental BICs can be realized in the open cavities with no symmetry like the open Sinai billiard in which the eigenmode of the resonator can become orthogonal to the continuum of the waveguide accidentally due to a smooth deformation of the eigenmode. We also review the one-dimensional systems in which the BICs occur owing to the fully destructive interference of two waves separated by spin or polarization or by paths in the Aharonov–Bohm rings. We make broad use of the method of effective non-Hermitian Hamiltonian equivalent to the coupled mode theory, which detects BICs by finding zero-width resonances.

Keywords: bound states in the continuum, wave localization in one-dimensional wires, open microwave and acoustic resonators, effective non Hermitian Hamiltonian

(Some figures may appear in colour only in the online journal)

1. Introduction

More than 2 centuries have passed since Thomas Young presented his well-known double-slit experiment which unambiguously proved the wave nature of light, but wave interference still offers unexplored phenomena in physics. Among the last ones to have attracted the close attention of researchers are the bound states in the continuum (BICs). In 1929, von Neumann and Wigner [1] claimed that the single-particle Schrödinger equation could possess localized solutions that correspond to isolated discrete eigenvalues embedded in the continuum of positive energy states for some artificial oscillating bounded potential. Extension and some correction of this work was done by Stillinger and Herrick [2], who presented a few examples of spherically symmetric attractive local potentials with the BICs of scattering states in the context of possible BICs in atoms and molecules (e.g., [3–6]). For a long time, the phenomenon was considered as a mathematical curiosity although the physical mechanism is very similar to the mechanism of the Anderson localization. The BIC as a localized state is a result of the precise destructive interference of waves scattered by the bounded potential in such a way that we have no outgoing wave.

The decisive breakthrough came with a paper by Friedrich and Wintgen [7], who formulated a general method to find BICs in quantum systems. The method based on the effective

*Author to whom any correspondence should be addressed.
Corresponding editor: Professor Masud Mansuripur.

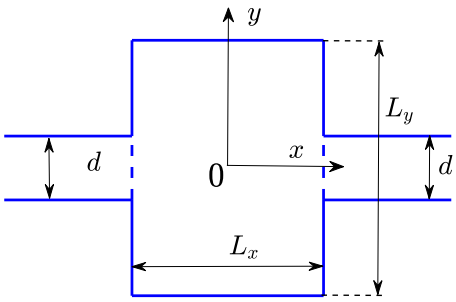

Figure 1. Two-dimensional plane resonator with two attached plane waveguides.

non-Hermitian Hamiltonian originates from the Feshbach unified theory of nuclear reactions [8, 9] and uses the fact that the occurrence of BICs is directly related to the phenomenon of the avoided level crossing. When two resonance states approach each other as a function of a certain continuous parameter, interference causes an avoided crossing of the two states in their energy positions and, for a certain value of the parameter, the width of one of the resonance states may vanish exactly. Since it remains above the threshold for decay into the continuum, this state becomes a BIC although each resonant state has a finite width. Numerous model considerations of different physical systems have since been presented [10–19].

The Fridrich–Wintgen (FW) approach of the effective Hamiltonian was first readily applied to a planar metallic integrable billiard (cavity) opened by attachment of two uniform plane waveguides [17] as shown in figure 1. Readers can find a description of the system in textbooks on electromagnetic (EM) fields (see, for example, [20]). It was shown that for the variation of the resonator width W, numerous events of degeneracy of the eigenmodes, say ψ_1 and ψ_2 , occur. Then, at the points of degeneracy, one can consider the superposed function $a\psi_1 + b\psi_2$. If each eigenmode is coupled with a waveguide first channel by means of W_1 and W_2 for the superposed function, we obviously have the coupling $aW_1 + bW_2$, which can be tuned to zero by the proper choice of the superposition coefficients a and b. That is an alternative interpretation of the BIC occurring at the degeneracy points in the integrable open resonators. The FW BICs were first experimentally observed by Lepetit and Kanté in metallic waveguide with two ceramic disks [21]. Similarly, Olendski and Mikhailovska have shown that in a curved 2D waveguide, a quasi-bound state formed as a result of the bend and at some critical parameters of the curve, it becomes a true bound state within the continuum [22]. Cattapan and Lotti have revealed BICs in a 2D straightforward stubbed quantum waveguide with impurities [23] and 2D serial structures [24]. Thus, it has been shown that going beyond 1D crucially increases opportunities for BICs.

The question of whether a wave can be perfectly confined (that is, whether a 'bound state' can exist) in an open system is related to a simple frequency criterion. If the frequency of a wave is outside the continuous spectral range spanned by the propagating waves, it can exist as a bound state because there is no pathway for it to radiate away. Conversely, a wave state with a frequency inside the continuous spectrum can only be a 'resonance' that leaks and radiates out to infinity. This is the conventional wisdom described in many books. A bound state in the continuum (BIC) is an exception to this conventional wisdom: it lies inside the continuum and coexists with extended waves, but it remains perfectly confined without any radiation.

Besides the Friedrich–Wintgen mechanism of fully destructive interference, other mechanisms for BICs exist. The most simple mechanism is symmetry protection. Bolsterli has treated a special case in which there occur discrete states in the continuum in separable potentials [25]. In such a system a symmetry incompatibility decouples the square-integrable eigenmodes from the propagating modes of the waveguides [26–28]. It is accepted to determine such BICs as the symmetry-protected (SP) ones. Less obvious but similar to the SP BICs are the accidental BICs, when in spite of absence of symmetry arguments, the coupling between the cavity eigenmode and the mode of the continuum can turn to zero accidentally by the variation of the shape of the cavity as it was demonstrated in an open Sinai billiard [29]. Firstly, such a possibility was mentioned by Friedrich and Wintgen in a paper on the physical realization of BICs in a hydrogen atom in a magnetic field [30]. Later, accidental BICs were demonstrated in photonic systems [31, 32].

A more sophisticated but transparent mechanism of BICs is Fabry–Perot (FP). Assume, we have two ideal metallic mirrors parallel to each other and with the distance L between them. All states are bounded in this system with the eigenfrequencies $\omega_n = \pi n/L, n = 1, 2, 3, \ldots$. If the mirrors have a finite transmission probability, all bound states become resonant states with finite line widths because of leakage through the mirrors [33]. Such a system is analogous to the simplest quantum mechanical problem of a single particle in double barrier potential. In this one-dimensional system, there are no BICs. However, in 1999 Kim and Satanin [34] put forward the idea of going beyond the one-dimensional case, applying temporally periodically driven barriers. Then, the effective dimensionality of the one-dimensional double barrier potential becomes two [35, 36] allowing for transmission zeros even for potential barriers of a finite height. The possibility of localizing the quantum particle in a tight-binding chain with an off-channel impurity driven by an ac field was later considered by Longhi and Della Valle in a series of papers on Floquet BICs [37–39].

Straightforward FP models which support BICs were considered by Fan *et al* [40] in the framework of coupled mode theory (CMT) [41]. In a series of papers [16, 42–44] two-dimensional identical quantum dots were used as FP mirrors. Then, the BICs were engineered by tuning the distance between the resonators coupled by wire. A similar approach was also used by Ordonez [45]. The same mechanism of BICs was exploited in photonic crystal systems [40, 46–49] in which one- and two-dimensional photonic crystals were used as perfectly reflecting mirrors. The occurrence of BICs in these systems is accompanied by the collapse of the Fano resonances when the transmission zero coalesces with the transmission unit [17, 21, 34]. Another variant of waveguides which supports BICs is the double bend waveguide [50], due to transmission zeros in the bend [22].

Up to now, I have briefly discussed bound states with discrete frequencies embedded into the waveguide continua which are quantized by the finite width of the waveguide (see figure 1). It is easy to realize the FW BIC embedded into the first continuum, which is separated from the next continua by afinite gap, for example a variation in the length of the resonator [17, 51–53] or the obstacle size in the waveguide [24, 54]. The state of the art is BICs embedded into a few continua of the waveguide [55]. At first glance it seems impossible to support BICs in the radiation continuum of free space given by a continuous spectrum of light line (cone) $\omega = ck$, where c is the light velocity. The closed metallic resonator in free space is an exceptional case because of its equivalence to quantum mechanical well potential with infinitely high walls. Similarly, there might be BICs in plasmonic nanostructures [56, 57]. This agrees with the theorem that there are no BICs in a bounded domain that is the complement of an unbounded domain [57, 58]. However, in infinite periodic arrays of dielectric particles, light can leak only into a discrete number of diffraction orders, allowing us to find BICs embedded into a finite number of diffraction continua [59–61]. Therefore the infinite periodic dielectric structures can support BICs, which has attracted the growing interest of the optical community because of the possibility of confining light. In this review I skip photonic BICs since they have already been the subject of recent reviews [62–66].

2. Applications of BICs

An orthogonality of BIC to the extended propagating states of the continuum, i.e. decoupling of the BIC from the continuum, is the reason for the existence of a localized state with discrete energy or frequency embedded into the continual spectrum [67]. In this view, the BIC is invisible to manipulation by probing incident fields also propagating in that continuum. At first glance, this renders BICs totally useless for practical purposes. However, if the scattering problem is granted an extra dimension by introducing a control parameter, one can immediately see that the traces of BICs emerge in the scattering spectrum as narrow Fano features once the control parameter is detuned from the BIC point transforming BIC into a quasi-BIC. The extremely high response of the quasi-BICs and the possibility of manipulating them has become extremely important in modern science and opens up many applications. I briefly review these applications although the list of them will hardly be exhaustive because of extensive ongoing theoretical and experimental studies of applications of BICs.

(a) **Lasing from BICs.** The high Q factor of the BICs enormously enhances the intensity of the EM fields in the resonators or near the zone of photonic crystal structures which support the bound states in the radiation continuum. The exploitation of the significant field enhancement of BICs to reduce the lasing threshold of miniaturised sources and boost their efficiency has been the subject of intense research. The first discussion of lasing from BICs in Γ-point of a two-dimensional periodical structure of InGaAsP quantum wells was reported by Kodigala *et al* [68]. Vortex lasing from BICs has also been demonstrated [69–72].

(b) **Sensing and biosensing.** The ability to detect biologically active molecules is of crucial importance for fundamental studies in biochemistry, applications in drug development, and point-of-care diagnostics. A broad class of label-free photonic biosensors exploits optical resonance effects. They experience a shift in the resonance frequency in response to a change of the refractive index of the medium surrounding the sensing area. Therefore BICs allow us to engineer optical sensors with a good sensitivity and an excellent figure of merit [73–78]. The sensitivity is affected by the spatial overlap between the non-radiating near field of the BIC and the surrounding cladding, while the figure of merit is proportional to the Q factor and ultimately represents the sensor capability to follow tiny changes in the environment refractive index [79–81].

(c) **Magneto-optics, optical dichroism, etc.** A magnetic circular dichroism near 100% from monolayer graphene has been achieved by use of BICs [82]. The rotationally symmetric chiral meta surfaces can support sharp resonances with the maximum optical chirality determined by precise shaping of BICs [83]. Being uncoupled from one circular polarization of light and resonantly coupled to its counterpart, a meta surface hosting the chiral BIC resonance exhibits a narrow peak in the circular dichroism spectrum with the quality factor limited by weak dissipation losses. Also assisted by the quasi-BICs with ultrahigh Q factors, the Goos–Hanchen shift [84] can be greatly enhanced to greater than or equal to four orders of wavelength [85], and the photonic spin Hall effect can be enhanced [86]. Next, it was shown that the infrared photoluminescence emission from Ge(Si) quantum dots enhanced with collective Mie modes of silicon nanopillars (BICs at Γ-point) results in strong reshaping of the photoluminescence spectra [87].

(d) **Enhancement of nonlinear effects and generation of the second harmonics.** With very few exceptions, nonlinear effects due to the Kerr effect in dielectric resonators are very small and require rather strong incident power. Therefore the straightforward possible applications of high-quality resonance modes such as BIC are found in the enhancement of the optical nonlinear effects [88–91]. One of the goals of any practical use of nonlinear effects is achieving efficient conversion of the fundamental frequency pump to the second harmonic signal [92]. Moreover, the SP BIC can convert many harmonics (the frequency comb) with a frequency step governed by the pumping power due to the coupling of the BIC mode with other modes that can emit into the continuum [93–103].

(e) **Light storage in BICs and release by demand.** For illumination of dielectric structures, the exact bound states in the radiation continuum have no effect in scattering of EM waves. However, owing to the Kerr effect, the BIC is coupled to other resonances of the structure that transform BICs into quasi-BICs whose decay time depends on

the intensity of incident light. Therefore, with illumination by a light pulse, this quasi-BIC traps some fraction of the pulse power, which remains preserved by the true BIC when the pulse passes the structure. The secondary pulse again couples the BIC with the radiation continuum and therefore releases storage power. These effects were shown in different structures supporting the SP BICs, the FW and FP BICs [104].

(f) **Routing and multiplexing via BICs.** As early as 1999, Fan *et al* [40] published general principles of channel drop processes (multiplexing). Propagating states can be transferred between the continuums through the double resonator system which supports the FP BICs. Later, the nonlinear mechanism of switching of channels was developed by use of the FW BICS in a single resonator positioned between two parallel waveguides [105]. More sophisticated schemes of resonators were proposed for experimental realization of multiplexing via the BICs in reference [106].

3. The effective non-Hermitian Hamiltonian

One powerful and unambiguous means to diagnose BICs is the method of effective non-Hermitian Hamiltonian [8, 107–111] which is equivalent to the CMT [41, 112]. An important advantage of the effective non-Hermitian Hamiltonian approach is the possibility of calculating the coupling matrix between closed system and continuum when the eigenmodes of subsystems are known [109, 113]. The approach of the effective non-Hermitian Hamiltonian [107–109] has found numerous applications in various branches of physics including atomic nuclei [110, 114], chaotic billiards [113, 115–119], tight-binding models [36, 111, 120–122], potential scattering [110], photonic crystals [123], etc.

The objective of the present paper is to revisit the concept of the effective non-Hermitian Hamiltonian in applications to open resonators with the Dirichlet or Neumann boundary conditions. The problem of resonant scattering typically involves a cavity (which could be quantum dot, microwave or acoustic cavity, etc) and scattering channels coupled to the cavity. The mainstream idea is to split the full Hilbert space into subspaces: subspace B formed by the eigenfunctions of discrete spectrum localized within the scattering center, and subspaces C which spans the extended eigenfunctions of the scattering channels. Therefore, the exact description of the open system meets a problem of matching the wave functions of discrete and continuous spectra. In 1958 Feshbach [8] introduced the idea of projecting the total Hilbert space onto the discrete states of subspace B. Operating on the Hamilton operator of the whole system

$$\widehat{H} = \widehat{H}_B + \sum_C (\widehat{H}_C + \hat{V}_{BC} + \hat{V}_{CB}) \tag{1}$$

with projection operators, Feshbach derived the effective non-Hermitian Hamiltonian [9]

$$\widehat{H}_{\text{eff}} = \widehat{H}_B + \sum_C \hat{V}_{BC} \frac{1}{E^+ - \widehat{H}_C} \hat{V}_{CB}. \tag{2}$$

Here, $\widehat{H}_B$ is the Hamiltonian of the closed system, $\widehat{H}_C$ is the Hamiltonian of the scattering channel C, $\hat{V}_{BC}$, $\hat{V}_{CB}$ stand for the coupling matrix elements between the eigenstates of closed cavity and the eigenstates of the scattering channels, and E is the energy of scattered particle (wave). An expression for the effective Hamiltonian (2) is easy to obtain through wave function presentation [107, 120, 124]:

$$|\Psi\rangle = \sum_b a_b |b\rangle + \int \mathrm{d}E' a(E')|E'\rangle. \tag{3}$$

Then we obtain two equations for expansion coefficients from the Scrödinger equation $\widehat{H}|\Psi\rangle = E|\Psi\rangle$,

$$\begin{aligned} \langle b|\widehat{H}|\Psi\rangle &= E_b a_b + \int \mathrm{d}E' a(E') V_b(E') = E a_b, \\ \langle E'|\widehat{H}|\Psi\rangle &= E' a(E') + \sum_b a_b V_b^*(E') = E a(E'), \end{aligned} \tag{4}$$

that give us the following equations:

$$a(E') = \frac{1}{E - E'} \sum_b a_b V_b(E') \tag{5}$$

and respectively

$$E_b a_b + \sum_{b'} \int \mathrm{d}E' \frac{V_b(E') V_b^*(E')}{E - E'} a_b'(E') = E a_b. \tag{6}$$

Equation (6) exactly corresponds to the eigenvalue problem in the subspace of discrete states of the closed system B: $\widehat{H}_{\text{eff}}|b\rangle = E|b\rangle$.

For an EM wave or acoustic transmission $E = \omega^2$, where ω is the frequency. The term $E^+ = E + \mathrm{i}0$ ensures that only outgoing waves will be present in the solution in scattering. As a result, the effective Hamiltonian (2) is a non-Hermitian matrix with complex eigenvalues z_λ which determine the positions and lifetimes of the resonant states as $\mathrm{Re}(z_\lambda)$, and $-2\,\mathrm{Im}(z_\lambda)$ [107, 109]. Assuming that the propagation band of the continuum is not bounded, then the effective non-Hermitian Hamiltonian takes the most simple form widely used in the scattering theory [108, 114, 117]:

$$\widehat{H}_{\text{eff}} = \widehat{H}_B - \mathrm{i} \sum_C \widehat{W}_C \widehat{W}_C^\dagger, \tag{7}$$

where $\widehat{W}_C$ is a column matrix whose elements account for the coupling of each individual inner state to the scattering channel C. The scattering matrix $\mathcal{S}_{CC'}$ is then given by the inverse of $E - \widehat{H}_{\text{eff}}$ [108, 117]:

$$\hat{S} = \delta_{CC'} - 2\mathrm{i} \widehat{W}^+ \frac{1}{\widehat{H}_{\text{eff}} - E + \mathrm{i}0} \widehat{W}, \tag{8}$$

where $C = \mathrm{L}, \mathrm{R}$. Therefore for the case of energy-/frequency-independent coupling matrix, the complex eigenvalues coincide with the poles of the S-matrix.

However this formulation of the effective Hamiltonian is oversimplified because of an unbounded spectrum of the continuum. Commonly the spectrum is bounded, at least below.

For example, the electron has the spectrum $E = \frac{\hbar^2 k^2}{2m}$ and EM waves have the spectrum $\omega = ck$. Although the form for the effective Hamiltonian (7) is preserved, the coupling matrix elements become dependent on the energy or frequency [111–113]. In what follows, we apply the method of the effective non-Hermitian Hamiltonian to several physical systems: (1) one-dimensional wires with off-channel cavities in the Aharonov–Bohm rings, (2) a two-dimensional microwave planar metallic waveguide consisting of the cavity and two attached waveguides and microelectronic waveguides (figure 1), and (3) three-dimensional acoustic cylindrical and spherical resonators with attached cylindrical waveguides.

4. Friedrich–Wintgen concept of BIC

One can see that the effective non-Hermitian Hamiltonian (7) consists of Hermitian part $\widehat{H}_B$ whose eigenvalues are the eigenfrequencies of the closed cavity and the second anti-symmetric imaginary part. This part is a result of the coupling of the cavity with the continua C of waveguides. The complex eigenvalues of the effective Hamiltonian have a clear physical meaning. Their real parts respond to the position of the resonances while their imaginary parts respond to the half resonant widths [107, 108]. In other words, if one prepares some field as the eigenmode of the closed cavity, it will decay because of the leakage of the mode into waveguides. Therefore the BIC is easily found out by turning one of the imaginary parts of the complex eigenvalues of the non-Hermitian effective Hamiltonian to zero, which was first established by Friedrich and Wintgen [7] in a generic two-level Hamiltonian. When two resonance states approach each other as a function of a certain continuous parameter, interferences cause an avoided crossing of the two states in their energy positions and, for a certain value of the parameter, the width of one of the resonance states vanishes exactly. Since it remains above the threshold for decay into the continuum, this state becomes a BIC. The Friedrich and Wintgen (FW) approach is significant in that it can be applicable to any waveguide system, in particular to microelectronic, microwave or acoustic resonators opened by the attachment of waveguides [17, 120, 125].

Let the cavity undergoes degeneracy, for example, the variation of shape. In the neighborhood of this degeneracy, it is reasonable to truncate the Hamiltonian of the cavity by only those eigenvalues, say E_1 and E_2, which are crossing. Moreover we assume that there is only one continuum with which the cavity modes are coupled. That gives the following two-level effective Hamiltonian:

$$\widehat{H}_{\text{eff}} = \begin{pmatrix} \epsilon - \mathrm{i}\gamma_1 & u - \mathrm{i}\sqrt{\gamma_1\gamma_2} \\ u - \mathrm{i}\sqrt{\gamma_1\gamma_2} & -\epsilon - \mathrm{i}\gamma_2 \end{pmatrix}, \tag{9}$$

where without loss of generality, we take $E_{1,2} = \pm\epsilon$. Also we introduce $\gamma_1 = W_1^2$, $\gamma_2 = W_2^2$ which could define the resonant widths of the levels $E_{1,2}$ if the effective Hamiltonian (9) was diagonal. $W_n, n = 1, 2$ are the coupling constants of the cavity modes in waveguide propagating mode. Parameter u is responsible for repulsion of the eigenfrequencies of the closed cavity due to, for example, an inner perturbation which removes the integrability of the cavity. For example, in section 7 we consider a hole inside the cavity transforming into a Sinai billiard where the eigenlevels are avoided.

The advantage of the two-level approximation is that the BIC can be considered analytically [12, 17]. Let us write the transmission amplitude in the biorthogonal basis of the eigenstates of the effective non-Hermitian Hamiltonian (9):

$$\widehat{H}_{\text{eff}}|\lambda) = z_\lambda|\lambda), \ (\lambda|\lambda') = \delta_{\lambda,\lambda'}, |\lambda) = |\lambda\rangle, \ (\lambda| = |\lambda)^c = \langle\lambda|^*, \tag{10}$$

i.e. the left states are related to the right states via transposing. Then using the condition of completeness

$$\sum_\lambda |\lambda)(\lambda| = 1$$

we can rewrite the transmission amplitude as sum of the resonant terms [111]:

$$T = -2\mathrm{i}\sum_\lambda \frac{V_\lambda^{\mathrm{L}} V_\lambda^{\mathrm{R}}}{E - z_\lambda} = -2\mathrm{i}\sum_\lambda \frac{V_\lambda^2}{E - z_\lambda}, \tag{11}$$

where $V_\lambda^C = V_\lambda, C = \mathrm{L}, \mathrm{R}$ are the coupling constants of resonant states with the continuum or the propagating mode of waveguides. Expression (11) immediately shows us that the complex eigenvalues z_λ are the poles of the S-matrix, provided that the matrix elements of the effective Hamiltonian are energy independent. Otherwise, we are to use the complex scaling method [126] or to solve nonlinear fixed point equations for real and imaginary parts of the complex eigenvalues z_λ, which define the resonant positions and the resonant widths [109]. The relation of V_λ with the coupling constants W_n of the states of closed cavity with waveguides will be given below. Let us first consider the integrable resonator with $u = 0$ shown in figure 1. Then

$$z_{1,2} = -\mathrm{i}\Gamma \pm \sqrt{(\epsilon - \mathrm{i}\Delta\Gamma)^2 - \gamma_1\gamma_2}, \tag{12}$$

where

$$\Gamma = \frac{\gamma_1 + \gamma_2}{2}, \qquad \Delta\Gamma = \frac{\gamma_1 - \gamma_2}{2}.$$

For simplicity we take the coupling constants of the cavity eigenmodes with the propagating mode of the waveguide equal, $\gamma_1 = \gamma_2$. Such an simplification substantially shortens the algebra of the eigenstates of the effective non-Hermitian Hamiltonian. Then the right eigenstates are

$$|1) = \frac{1}{\sqrt{2\eta(\eta + \mathrm{i}\epsilon)}}\begin{pmatrix} -\gamma \\ \eta + \mathrm{i}\epsilon \end{pmatrix}, \ |2) = \frac{1}{\sqrt{2\eta(\eta - \mathrm{i}\epsilon)}}\begin{pmatrix} \gamma \\ \eta - \mathrm{i}\epsilon \end{pmatrix} \tag{13}$$

with corresponding eigenvalues

$$z_{1,2} = -\mathrm{i}\gamma \pm \eta, \tag{14}$$

where $\eta = \sqrt{\gamma^2 - \epsilon^2}$. Let us write the following identity

$$\widehat{W} = \widehat{W}\sum_\lambda |\lambda)\left(\lambda| = \sum_\lambda V_\lambda|\lambda\right), \tag{15}$$

where V_λ is the coupling constants between the resonant states and the continuum. Therefore from equation (13), we obtain

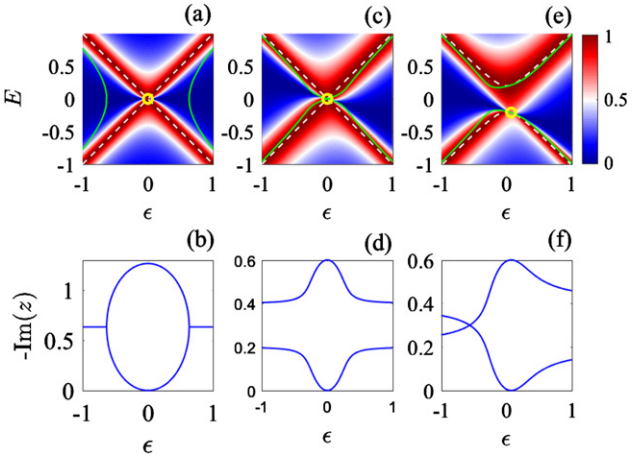

Figure 2. The transmittance, eigenlevels of a closed system (dashed white lines), resonant positions (solid green lines), resonant widths (solid lines, below) and BICs (open circles) in a two-level description of the effective Hamiltonian (9). (a) and (b) $\gamma_1 = \gamma_2 = 0.1, u = 0$; (c) and (d) $\gamma_1 = 0.1, \gamma_2 = 0.2, u = 0$; (e) and (f) $\gamma_1 = 0.1, \gamma_2 = 0.2, u = 25$.

the link between coupling constants W_n, where n enumerates the closed resonator states and V_λ, where λ enumerates the resonant states:

$$V_1 = \frac{W}{\sqrt{2\eta(\eta + \mathrm{i}\epsilon)}}(\eta + \mathrm{i}\epsilon - \gamma), \quad V_2 = \frac{W}{\sqrt{2\eta(\eta - \mathrm{i}\epsilon)}}(\eta - \mathrm{i}\epsilon + \gamma), \tag{16}$$

where $W = W_1 = W_2$.

The BIC occurs when $\epsilon = 0$. The eigenstates are limited to

$$|1\rangle = \frac{1}{\sqrt{2}}\begin{pmatrix}-1\\1\end{pmatrix}, \qquad |2\rangle = \frac{1}{\sqrt{2}}\begin{pmatrix}1\\1\end{pmatrix}. \tag{17}$$

From equation (16), one can see that the resonant state $|1\rangle$ decouples from the continuum at $\epsilon = 0$ while the state $|2\rangle$ acquires maximal coupling with the continuum (superradiant state). Therefore the state $|1\rangle$ can be qualified as the FW BIC decoupled from the continuum owing to the exact destructive interference of leaking eigenmodes of the closed cavity $|1\rangle$ and $|2\rangle$. For such a simplified case of equal coupling constants and $u = 0$, we see the difference between the FW BIC, which is $V_1(\epsilon = 0) = 0$ with respect to the eigenstates $|\lambda\rangle$ of $\widehat{H}_{\mathrm{eff}}$ and the SP BIC which has $W_1 = 0$ with respect to the eigenstate of $\widehat{H}_B$ of the closed cavity. The general case of N levels was considered in [67], where it is proved that decoupling from all channels of the continuum described is a necessary and sufficient condition for a resonance state to be the BIC, i.e. the state with vanishing decay width.

The transmittance is plotted in figure 2(a), which demonstrates that at the BIC point $E = 0, \epsilon = 0$ the maximal transmittance coalesces with the maximal reflectance (collapse of the Fano resonance [34]). Simultaneously at the BIC point, we observe in figure 2(b) that the resonant width turns to zero.

Let consider the transmittance in the vicinity of the BIC's point $\epsilon = 0, E = 0$. The eigenvalues of $\widehat{H}_{\mathrm{eff}}$ can be approximated as $z_1 \approx -\mathrm{i}\epsilon^2/2\Gamma, z_2 \approx -2\mathrm{i}\Gamma$. Then the transmission amplitude (11) takes the simple form

$$T(E, \epsilon) \approx -\frac{2\mathrm{i}E\Gamma}{2E\Gamma + \mathrm{i}\epsilon^2}. \tag{18}$$

It follows $|T| = 0$ for $E = 0, \epsilon \neq 0$, and $|T| = 1$ for $\epsilon = 0$, $E \neq 0$. Therefore, the BIC is a singular point in the sense that the value of the transmission amplitude depends on the way to approach this point. If $\Delta\Gamma \neq 0$ the transmission zero follows $E = \epsilon\Delta\Gamma/\Gamma$. In the general case of different coupling constants γ_1, γ_2 and $u \neq 0$ we will follow Kikkawa *et al* [127]. We have for the eigenvalues of the effective Hamiltonian (9)

$$(z + \epsilon + \mathrm{i}\gamma_1)(z - \epsilon + \mathrm{i}\gamma_2) - (u - \mathrm{i}\sqrt{\gamma_1\gamma_2})^2 = 0. \tag{19}$$

Then we have for the roots of this equation according to the Vietta's formula

$$\begin{aligned} z_1 + z_2 &= -\mathrm{i}(\gamma_1 + \gamma_2), \\ z_1 z_2 &= -(\epsilon + \mathrm{i}\gamma_1)(\epsilon - \mathrm{i}\gamma_2) - (u - \mathrm{i}\sqrt{\gamma_1\gamma_2})^2 \\ &= -\epsilon^2 - u^2 + 2\mathrm{i}(u\sqrt{\gamma_1\gamma_2} - \epsilon(\gamma_1 - \gamma_2)). \end{aligned} \tag{20}$$

At the BIC's point one of the roots, say z_1, is real. In that case, the roots can be expressed using real quantities A and B as

$$\begin{aligned} z_1 &= A, \\ z_2 &= B - \mathrm{i}(\gamma_1 + \gamma_2). \end{aligned} \tag{21}$$

Substitution of equation (21) into equation (20) gives

$$\begin{aligned} A + B &= 0, \\ AB &= -\epsilon^2 - u^2. \end{aligned} \tag{22}$$

On the other hand, by comparing the imaginary parts of both sides of equation (20) we obtain

$$A = -\frac{\epsilon(\gamma_1 - \gamma_2) + 2u\sqrt{\gamma_1\gamma_2}}{\gamma_1 + \gamma_2}. \tag{23}$$

Finally from equations (22) and (23) we obtain the following equation for the BIC's point:

$$u(\gamma_1 - \gamma_2) = 2\epsilon\sqrt{\gamma_1\gamma_2}. \tag{24}$$

First, this equation for the BIC point in a two-level approximation was obtained by Volya and Zelevinsky [12], and the solution is shown in figures 2(e) and (f).

5. Application to one-dimensional structures

5.1. Potential well

Let us consider the textbook problem of quantum particle propagation in a one-dimensional potential relief like shown in figure 1 of a review by Hsu *et al* [62]. The wave functions in the segments of the structure are the following:

$$\begin{aligned} \psi_{\mathrm{L}}(x) &= \exp(\mathrm{i}kx) + r\,\exp(-\mathrm{i}kx), \\ \psi(x) &= a\,\exp(\mathrm{i}qx) + b\,\exp(-\mathrm{i}qx), \\ \psi_{\mathrm{R}}(x) &= t\,\exp(\mathrm{i}kx). \end{aligned} \tag{25}$$

By using the boundary conditions, we can write the following equation for the solution:

$$\hat{L}\vec{\psi} = \vec{g}, \tag{26}$$

where $\hat{L}(k)$ is the following matrix:

$$\begin{pmatrix} -1 & 1 & 1 & 0 \\ k & q & -q & 0 \\ 0 & \mathrm{e}^{\mathrm{i}qL} & \mathrm{e}^{-\mathrm{i}qL} & -\mathrm{e}^{\mathrm{i}kL} \\ 0 & q\,\mathrm{e}^{\mathrm{i}qL} & -q\,\mathrm{e}^{-\mathrm{i}qL} & -0\,\mathrm{e}^{\mathrm{i}kL} \end{pmatrix}, \tag{27}$$

$\vec{g}^{\mathrm{T}} = (1\ k\ 0\ 0)$, $\vec{\psi}^{\mathrm{T}} = (r\ a\ b\ t)$, and L is the width of the potential well. The determinant of matrix $\hat{L}(k)$ equals

$$2\mathrm{i}(k^2 + q^2)\sin(kL) + 4kq\,\cos(kL), \tag{28}$$

which is the denominator of the S-matrix [128], zeros of which define its poles. The BIC is the solution of the inhomogeneous part of equation (26) when $\vec{g} = 0$. In order for there to be a BIC, the determinant (28) is to be turn to zero, which cannot be fulfilled for the case of a one-dimensional potential well. Therefore the one-dimensional potential cannot support localized states with energy embedded into the continuum of extended states with $E > 0$. This is the conventional wisdom described in many books. A bound state in the continuum (BIC) is an exception to this conventional wisdom: it lies inside the continuum and coexists with extended waves, but it remains perfectly confined without any leakage. In 1929, von Neumann and Wigner [1] discovered that the long-range oscillating attractive one-dimensional potential can support BICs. The BIC is a classical paradox of a quantum particle with enough energy to leak from the potential well and nevertheless remaining spatially confined. The Neumann–Wigner BIC emerges due to precise destructive interference of waves scattered by a bound potential in such a way that we obtain a localized state. The physics of localization is similar to Anderson localization in random potential [129]. For a long time, the phenomenon was considered as a mathematical curiosity because potentials such as those invented by von Neumann and Wigner (corrections of the potentials were done by Stillinger [2]) can hardly be realized experimentally.

5.2. BICs in Aharonov–Bohm rings

The Aharonov–Bohm oscillations of conductance are another bright example of wave interference when an electron encircling upper or down arms of ring acquires additional magnetic flux phases $\pm\gamma/2$ where $\gamma = 2\pi\Phi/\Phi_0, \Phi = B\pi R^2$ is the magnetic flux, $\Phi_0 = 2\pi\hbar c/e$ [130]. In this subsection we show that particular case of fully destructive interference gives rise to the localization of electron inside the ring, i.e. BICs [131].

Following Xia [132] we write the wave functions in the segments of the structure shown in figure 3(a) as

$$\begin{aligned} \psi_1(x) &= \exp(\mathrm{i}kx) + r\,\exp(-\mathrm{i}kx), \\ \psi_2(x) &= a_1\,\exp(\mathrm{i}k^-x) + a_2\,\exp(-\mathrm{i}k^+x), \\ \psi_3(x) &= b_1\,\exp(\mathrm{i}k^+x) + b_2\,\exp(-\mathrm{i}k^-x), \\ \psi_4(x) &= t\,\exp(\mathrm{i}kx), \end{aligned} \tag{29}$$

where $k^- = k - \gamma, k^+ = k + \gamma$. All variables are dimensionless via the ring length $2\pi R$. The boundary conditions (the continuity of the wave functions and the conservation of the current density) allow us to find all coefficients in (29). We write the corresponding equation in matrix form

$$\hat{F}\vec{\psi} = \vec{g}, \tag{30}$$

where $\hat{F}(k,\gamma)$ is the following matrix

$$\begin{pmatrix} -1 & 0 & 1 & 1 & 0 & 0 \\ -1 & 0 & 0 & 0 & 1 & 1 \\ 0 & -1 & \mathrm{e}^{\mathrm{i}k^-/2} & \mathrm{e}^{-\mathrm{i}k^+/2} & 0 & 0 \\ 0 & -1 & 0 & 0 & \mathrm{e}^{\mathrm{i}k^+/2} & \mathrm{e}^{-\mathrm{i}k^-/2} \\ 1 & 0 & \dfrac{k^-}{k} & -\dfrac{k^+}{k} & \dfrac{k^+}{k} & -\dfrac{k^-}{k} \\ 0 & -1 & \dfrac{k^-}{k}\,\mathrm{e}^{\mathrm{i}\frac{k^-}{2}} & -\dfrac{k^+}{k}\,\mathrm{e}^{-\mathrm{i}\frac{k^+}{2}} & \dfrac{k^+}{k}\,\mathrm{e}^{\mathrm{i}\frac{k^+}{2}} & -\dfrac{k^-}{k}\,\mathrm{e}^{-\mathrm{i}\frac{k^-}{2}} \end{pmatrix}, \tag{31}$$

$\vec{g}^{\mathrm{T}} = (1\ 1\ 0\ 0\ 1\ 0)$. The vector $\vec{\psi}^{\mathrm{T}} = (r\ t\ a_1\ a_2\ b_1\ b_2)$ is the solution for the scattering wave function:

$$\begin{aligned} r &= 2(3\,\cos\,k - 4\,\cos\,\gamma + 1)/Z, \\ t &= 16\mathrm{i}\left(\sin\frac{k}{2}\,\cos\frac{\gamma}{2}\right)/Z, \\ a_1 &= 2(2\,\mathrm{e}^{\mathrm{i}\gamma} - 3\,\mathrm{e}^{-\mathrm{i}k} + 1)/Z, \\ a_2 &= 2(\mathrm{e}^{\mathrm{i}k} + 1 - 2\,\mathrm{e}^{\mathrm{i}\gamma})/Z, \\ Z &= 8\,\cos\,\gamma - 9\,\mathrm{e}^{-\mathrm{i}k} - \mathrm{e}^{\mathrm{i}k} + 2, \end{aligned} \tag{32}$$

$b_{1,2}(k,\gamma) = a_{1,2}(k,-\gamma)$. In figure 3 we show lines of the transmission zeros ($|t(k,\gamma)| = 0$, dashed lines) which cross the lines of the transmission ones ($|t(k,\gamma)| = 1$, solid lines) at points

$$\begin{aligned} k_m &= 2\pi m, \quad m = \pm1, \pm2, \ldots, \\ \gamma_n &= 2\pi n, \quad n = 0, \pm1, \pm2, \ldots. \end{aligned} \tag{33}$$

As can be seen from the expression of the denominator Z in equation (32), the imaginary part of the poles vanishes at these points. Simultaneously, a degeneracy of eigen energies of a closed ring $(k_m - \gamma)^2$ occurs at these points. Here m is the azimuthal index (magnetic quantum number) that defines the eigenfunctions of the closed ring $\psi_m(x) = \exp(\mathrm{i}k_m x)$. The point $k = 0$ is excluded from the consideration since it gives zero conductance. The existence of the peculiar points (33) was shown in [14] as points where the density of states shows similar collapses as those of the Fano resonance in transmission. To show that the BICs appear at these points (33), let us consider one of the points, say, $\mathbf{s}_0 = (k_1, \gamma_1) = 2\pi(1,1)$. All the other points are equivalent because of the periodical dependence of the system on k and γ. In the vicinity of the point $\mathbf{s}_0$, we write equation (32) in the following approximated form:

$$\begin{aligned} t &\approx \frac{\Delta k}{\Delta k + \mathrm{i}(\Delta\gamma)^2/2}, & r &\approx \frac{\mathrm{i}(3\Delta k^2 - 4\Delta\gamma^2)}{4(2\Delta k + \mathrm{i}\Delta\gamma^2)}, \\ a_1 &\approx \frac{3\Delta k + 2\Delta\gamma}{4\Delta k + 2\mathrm{i}\Delta\gamma^2}, & a_2 &\approx \frac{\Delta k - 2\Delta\gamma}{4\Delta k + 2\mathrm{i}\Delta\gamma^2}, \end{aligned} \tag{34}$$

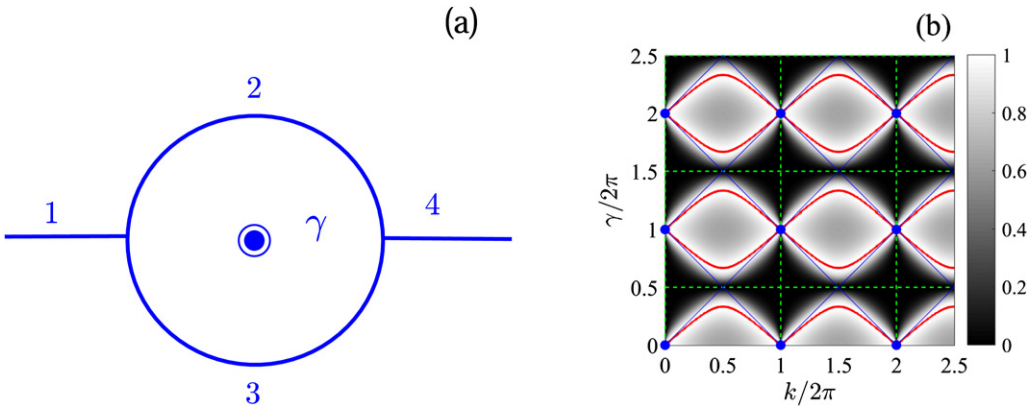

Figure 3. (a) One-dimensional ring thread by the magnetic flux γ and opened by attachment of two leads. (b) Transmission through the ring vs the magnetic flux and wave number $k = \sqrt{E}$. Green dashed lines show transmission zeros $|t|^2 = 0$ and solid red lines show transmission ones $|t|^2 = 1$. The BICs are marked by blue closed circles. Thin blue solid lines show wave numbers as dependent on the flux $k = (m - \gamma)$ where m are integers. Reprinted by permission from Springer Nature Customer Service Centre GmbH: JETP Letters [131] © 2006.

where $\Delta k = k - k_1, \Delta\gamma = \gamma - \gamma_1$. The transmission amplitude in the vicinity of the BIC point $\mathbf{s}_0$ in (34) is similar to the expressions obtained for a shifted von Neumann–Wigner potential [4] or the two-level approximated approach (see equation (18)). One can see that all amplitudes $a_{1,2}, b_{1,2}$ of the inner wave functions are singular at the point $\mathbf{s}_0$. Such a result for the BIC points was firstly found by Pursey and Weber [4]. At this point the matrix (31) takes the following form:

$$\hat{F}(\mathbf{s}_0) = \begin{pmatrix} -1 & 0 & 1 & 1 & 0 & 0 \\ -1 & 0 & 0 & 0 & 1 & 1 \\ 0 & -1 & 1 & 1 & 0 & 0 \\ 0 & -1 & 0 & 0 & 1 & 1 \\ 1 & 0 & 0 & -2 & 2 & 0 \\ 0 & -1 & 0 & -2 & 2 & 0 \end{pmatrix}. \tag{35}$$

The determinant of the matrix $\hat{F}(\mathbf{s}_0)$ equals zero. Therefore, $\hat{F}\vec{f}_0 = 0$. By direct substitution of the vector $\vec{f}_0^{\,\mathrm{T}} = \frac{1}{2}(0\ 0\ 1\ -1\ -1\ 1)$ one can verify that $\vec{f}_0$ is the right eigenvector, which is the null vector. The corresponding left null eigenvector is $\tilde{\vec{f}}_0 = \frac{1}{2}(-1\ 1\ 1\ -1\ 0\ 0)$. It is well known from linear algebra that if the determinant of matrix $\hat{F}$ is equaled to zero, then the necessary and sufficient condition for the existence of a solution of the equation (30) is that the vector $\tilde{\vec{f}}_0$ is orthogonal to vector $\vec{g}$ [133]. In holds, indeed, that $\tilde{\vec{f}}_0 \cdot \vec{g} = 0$. Therefore, the null vector $\tilde{\vec{f}}_0$ is proven to be the BIC. The general solution of equation (30) at the point $\mathbf{s}_0$ can therefore be presented as

$$\vec{\psi}(\mathbf{s}_0) = \alpha\vec{f}_0 + \vec{\psi}_p, \tag{36}$$

where α is an arbitrary coefficient and $\vec{\psi}_p$ is particular transport solution of equation (30). By direct substitution one can verify that $\vec{\psi}_p^{\,\mathrm{T}} = \left(0\ 1\ \frac{3}{4}\ \frac{1}{4}\ \frac{3}{4}\ \frac{1}{4}\right)$ is the particular solution of equation (30). It is worthwhile to note that this result completely agrees with the scattering theory on graphs [134, 135]. Texier has shown that for certain graphs, the stationary scattering state gives the solution of the Schrödinger equation for the continuum spectrum separately for a discrete set of energies where some additional states are localized in the graph and thus are not probed by scattering, leading to the failure of the state counting method from the scattering.

5.3. Zeeman localization

Although when open the Aharonov–Bohm ring consists of 1D wires, the ring is two-dimensional in order for the electron to encircle the flux. In this subsection we present the model which is indeed one-dimensional but capable of localizing the electron. We go beyond the scalar Helmhotz equation and employ the interference of spin-polarized resonant states of the one-dimensional electron transmission [136]. Let us consider three domains in which an external stationary magnetic field is applied as sketched in figure 4. We assumethat the external magnetic field $\vec{B}$ inside the central layer is tilted relative to the outer magnetic field oriented along the z-axis. We also assume that the inner layer has the potential shifted relative to the outer layers by a value U_0. Outside of the central layer, the electron has two split energy spectra $E = k_\sigma^2 \mp B,\ \sigma = \uparrow, \downarrow$ which specify the continua by the wave vector $\vec{k}_\sigma$. In the central layer, the spin-dependent spectra have the form $E = q_s^2 + U_0 \mp B,\ s = 1, 2$, which specify spin-dependent channels by the vector $\vec{q}_s$. Owing to choice of the potential step ($U_0 = -20$) as depicted in figure 4 in green, both spin channels being open in the central layer while outside only the spin up continuum is open for $E < B$, only the electron with spin up participates in electron transmission and reflection.

Let us write the Schrödinger equation for the toy model of electron in magnetic field (see figure 4):

$$\left[\frac{1}{2m}\left(\mathrm{i}\hbar\nabla + \frac{e}{c}\mathbf{A}\right)^2 + U_0(z) - \sigma\mathbf{B}(z) - E\right]\Psi = 0. \tag{37}$$

The orbital motion has characteristic length $a_B^2 = \frac{\hbar c}{eB}$, which in the magnetic field of 10^3Oe equals 100 nm. Then for layer of thickness $L \ll a_B$, we can disregard the orbital contribution in equation (37) and rewrite it as follows:

$$\left[\nabla^2 - U_0(z) + \sigma\mathbf{B}(z) + E\right]\Psi = 0. \tag{38}$$

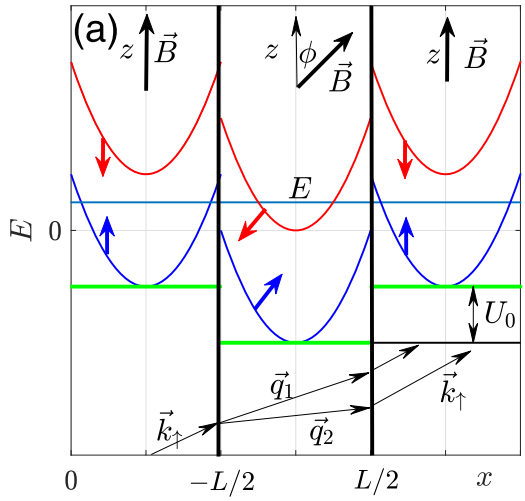

Figure 4. An one-dimensional spin model for illustration of BICs due to the fully destructive interference of spin-polarized resonant states. Beyond the central layer, the magnetic field $\vec{B}$ is directed along the z-axis; inside the central layer $\vec{B}$ is tilted by angle ϕ. The spin-up electron falls by angle θ with the energy below the spectrum of spin-down and splits into two states specified by $\vec{k}_1$ and $\vec{k}_2$. Reproduced from [136]. CC BY 4.0.

Next we substitute the step-wise magnetic filed as shown in figure 4. Then Hamiltonian (38) will take the following form:

$$\widehat{H} = \begin{cases} -\dfrac{\mathrm{d}^2}{\mathrm{d}z^2} - \sigma_x B & \text{if } |z| > L/2; \\ -\dfrac{\mathrm{d}^2}{\mathrm{d}z^2} + U_0 - \sigma_x B\cos(\phi) - \sigma_z B\sin(\phi) & \text{if } |z| < L/2. \end{cases} \tag{39}$$

In the outer layers, which form the radiation continua, with the following propagating solutions

$$\Psi_{\vec{k}_\sigma}(\vec{x}) = \exp(\mathrm{i}\vec{k}_\sigma\vec{x})|\sigma\rangle, \tag{40}$$

where $\sigma = \uparrow, \downarrow$,

$$|\uparrow\rangle = \begin{pmatrix} 1 \\ 0 \end{pmatrix}, \qquad |\downarrow\rangle = \begin{pmatrix} 0 \\ 1 \end{pmatrix}, \tag{41}$$

and

$$E = k_\sigma^2 \mp B. \tag{42}$$

Respectively for the inner layer we have

$$\Psi_{\vec{q}_s}(\vec{x}) = \exp(\mathrm{i}\vec{q}_s\vec{x})|s\rangle, \tag{43}$$

where $s = 1, 2$,

$$|1\rangle = \begin{pmatrix} \cos(\phi/2) \\ \sin(\phi/2) \end{pmatrix}, \qquad |2\rangle = \begin{pmatrix} -\sin(\phi/2) \\ \cos(\phi/2) \end{pmatrix}, \tag{44}$$

and

$$E = q_s^2 + U_0 \mp B. \tag{45}$$

Let us choose the energy of incident electron that only spin up channel is open. Then at the left ($z < -L/2$) we have

$$\Psi_{\mathrm{L}}(\vec{x}) = (\mathrm{e}^{\mathrm{i}\vec{k}_\uparrow\vec{x}} + r_\uparrow \mathrm{e}^{-\mathrm{i}\vec{k}_\uparrow\vec{x}})|\uparrow\rangle. \tag{46}$$

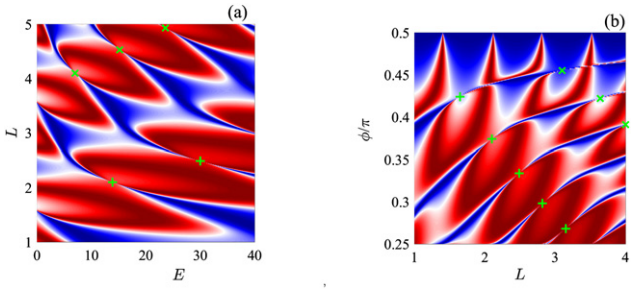

Figure 5. Reflection probability of the spin-up electron for $B = 10$ tilted by angle $\phi = \pi/3$ and $U_0 = -20$ vs (a) incident energy E and central layer thickness L at angle of incidence $\theta = \pi/4$, and (b) vs angle of incidence θ and L at incident energy $E = 30$ and $\phi = \pi/4$. Green plus symbols mark the points of the BICs symmetric with respect to the center of the layer, while times symbols mark the points of antisymmetric BICs. Reproduced from [136]. CC BY 4.0.

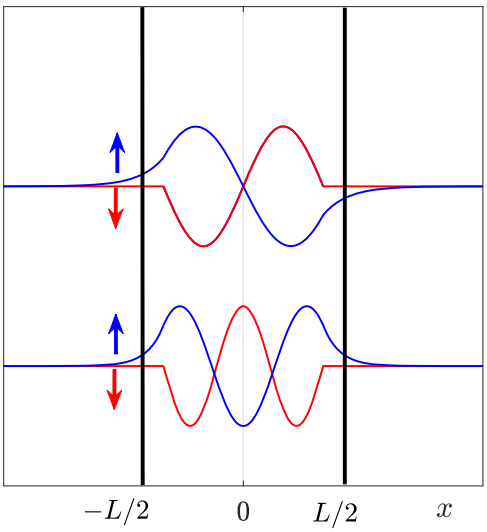

Figure 6. The BIC solutions, symmetric and antisymmetric, in the layered structure.

Inside the defect layer ($|z| < L/2$) both channels are open due to proper choice of the potential $U_0 = -20$ and therefore one can present the solutions as follows

$$\Psi_B(\vec{x}) = \sum_{s=1,2} (a_s\,\mathrm{e}^{\mathrm{i}\vec{q}_s\vec{x}} + b_s\,\mathrm{e}^{-\mathrm{i}\vec{q}_s\vec{x}})|s\rangle. \tag{47}$$

Finally, at the right side ($z > L/2$) we write

$$\Psi_{\mathrm{R}}(\vec{x}) = t_\uparrow\,\mathrm{e}^{\mathrm{i}\vec{k}_\uparrow\vec{x}}|\uparrow\rangle. \tag{48}$$

Here $r_\uparrow$ and $t_\uparrow$ are the reflection and transmission amplitudes. Next, assume an electron with spin σ incidents with wave vector $\vec{k}_\sigma = (k_{x\sigma}, k_{z\sigma})$ and reflecting with the reflection amplitude r_σ. Because of the preservation of the transverse component of moment $k_{x\sigma} = k_{xs} = k_x$ we obtain the following equations:

$$1 + r_\uparrow = (a_1 + b_1)\cos(\phi/2) - (a_2 + b_2)\sin(\phi/2),$$
$$k_{z\uparrow}(1 - r_\uparrow) = q_{z1}(a_1 - b_1)\cos(\phi/2) - q_{z2}(a_2 - b_2)\sin(\phi/2),$$
$$r_\downarrow = (a_1 + b_1)\sin(\phi/2) + (a_2 + b_2)\cos(\phi/2),$$

Table 1. Quantum/optical correspondence. Reproduced from [136]. CC BY 4.0.

Quantum mechanics	Optics
Electron	Photon
$\psi, \frac{\partial \psi}{\partial z}$	**E**,**B**
Spin	Polarization
Energy	Frequency
$\vert\downarrow\rangle$	TE-wave
$\vert\uparrow\rangle$	TM-wave
Magnetic field	Anisotropy axis

$$
\begin{aligned}
-k_{z\downarrow} r_{\downarrow} &= q_{z1}(a_1 - b_1)\sin(\phi/2) \\
&\quad + q_{z2}(a_2 - b_2)\cos(\phi/2), \\
t_{\uparrow}\, \mathrm{e}^{\mathrm{i}k_{z\uparrow}L} &= (a_1\, \mathrm{e}^{\mathrm{i}q_{z1}L} + b_1\, \mathrm{e}^{-\mathrm{i}q_{z1}L})\cos(\phi/2) \\
&\quad - (a_2\, \mathrm{e}^{\mathrm{i}q_{z2}L} + b_2\, \mathrm{e}^{-\mathrm{i}q_{z2}L})\sin(\phi/2), \\
k_{z\uparrow} t_{\uparrow}\, \mathrm{e}^{\mathrm{i}k_{z\uparrow}L} &= q_{z1}(a_1\, \mathrm{e}^{\mathrm{i}q_{z1}L} - b_1\, \mathrm{e}^{-\mathrm{i}q_{z1}L})\cos(\phi/2) \\
&\quad - q_{z2}(a_2\, \mathrm{e}^{\mathrm{i}q_{z2}L} - b_2\, \mathrm{e}^{-\mathrm{i}q_{z2}L})\sin(\phi/2), \\
t_{\downarrow}\, \mathrm{e}^{\mathrm{i}k_{z\downarrow}L} &= (a_1\, \mathrm{e}^{\mathrm{i}q_{z1}L} + b_1\, \mathrm{e}^{-\mathrm{i}q_{z1}L})\sin(\phi/2) \\
&\quad + (a_2\, \mathrm{e}^{\mathrm{i}q_{z2}L} + b_2\, \mathrm{e}^{-\mathrm{i}q_{z2}L})\cos(\phi/2), \\
k_{z\downarrow} t_{\downarrow}\, \mathrm{e}^{\mathrm{i}k_{z\downarrow}L} &= q_{z1}(a_1\, \mathrm{e}^{\mathrm{i}q_{z1}L} - b_1\, \mathrm{e}^{-\mathrm{i}q_{z1}L})\sin(\phi/2) \\
&\quad + q_{z2}(a_2\, \mathrm{e}^{\mathrm{i}q_{z2}L} - b_2\, \mathrm{e}^{-\mathrm{i}q_{z2}L})\cos(\phi/2). \qquad (49)
\end{aligned}
$$

The transmission probability versus the thickness of potential well L and incident energy or angle of incidence θ is plotted in figures 5(a) and (b) respectively, where one can see typical points for BICs when the collapse of the Fano resonance is observed. These points unambiguously indicate the BIC points. Indeed, the BIC as a localized mode inside the layer can be found from the equations of continuity at the interfaces. These equations can be simplified with account of symmetry relative to $z \to -z$. Then the symmetric BIC can be written as

$$
\psi_{\mathrm{BIC,sym}}(z) = \begin{cases} a\, \cos(q_{z1}z)|1\rangle + b\, \cos(q_{z2}z)|2\rangle & \text{if } |z| < L/2 \\ c\, \mathrm{e}^{(-|k_{z\downarrow}|z)}|\downarrow\rangle & \text{if } |z| > L/2, \end{cases} \qquad (50)
$$

where the last contribution is the result of evanescent mode with spin down and asymmetric BIC:

$$
\psi_{\mathrm{BIC,asym}}(z) = \begin{cases} a\, \sin(q_{z1}z)|1\rangle + b\, \sin(q_{z2}z)|2\rangle & \text{if } |z| < L/2 \\ \mathrm{sign}(z) c\, \mathrm{e}^{(-|k_{z\downarrow}|z)}|\downarrow\rangle & \text{if } |z| > L/2. \end{cases} \qquad (51)
$$

We imply that the modes equal zero at the spin up continuum and obey the continuity equations for the evanescent mode spin down. As a result, we obtain the following equations for the symmetric BIC:

$$
\begin{aligned}
&a\, \cos(\phi/2)\cos(q_{z1}L/2) - b\, \sin(\phi/2)\cos(q_{z2}L/2) = 0, \\
&a\, \sin(\phi/2)\cos(q_{z1}L/2) + b\, \cos(\phi/2)\cos(q_{z2}L/2) = c\, \mathrm{e}^{(-|k_{z\downarrow}|L/2)}, \qquad (52) \\
&aq_{z1}\, \sin(\phi/2)\sin(q_{z1}L/2) + bq_{z2}\, \cos(\phi/2)\sin(k_{z2}L/2) = c|k_{z\downarrow}|\mathrm{e}^{(-|k_{z\downarrow}|L/2)}.
\end{aligned}
$$

Thus, we obtain the following equation for the symmetric BIC points:

$$
-\tan^2(\phi/2) = \frac{q_{z2}\, \tan(q_{z2}L/2) - |q_{z\downarrow}|}{k_{z1}\, \tan(q_{z1}L/2) - |k_{z\downarrow}|}, \qquad (53)
$$

and respectively for the asymmetric BIC points:

$$
-\tan^2(\phi/2) = \frac{q_{z2}\, \cot(q_{z2}L/2) + |k_{z\downarrow}|}{q_{z1}\, \cot(q_{z1}L/2) + |k_{z\downarrow}|}. \qquad (54)
$$

The solutions of equations (52) and (53) are marked in figure 5 by pluses and times symbols respectively which exactly coincide with points of the Fano resonance collapse. The lowest symmetric and antisymmetric BIC solutions are shown in figure 6.

In table 1 we establish the one-by-one correspondence between the spin of the electron and the polarization state of light. This comes about because the BICs were verified experimentally by fully destructive interference of light paths with TM and TE polarizations in the anisotropic layer [136].

6. BICs in two-dimensional planar open cavities

Two- and three-dimensional wave transmission through cavities is distinct to one-dimensional transmission. First, by changing the shape of the 2D or 3D cavity we can achieve a degeneracy in the 1D resonator and therefore avoid the crossing of resonances. Second, 2D and 3D waveguides attached to the 2D and 3D cavities can support a finite number of open channels and is dependent on wave frequency. The other channels are closed forming evanescent modes whose role is crucially important for BICs. The evanescent modes of the waveguide shift the BIC points and 'blow out' the BIC modes from the open resonator. Moreover in 3D resonators the evanescent modes play a principal role in giving rise to the BICs.

In order to illustrate these statements, we start with the planar microwave metallic cavity or resonator with the Dirihclet boundary conditions at the walls. Such a system is convenient in that the solutions with different polarizations, TE and TM, are separated [137]. The total system can be viewed as consisting of three subsystems: two semiinfinite planar waveguides and rectangular plane resonator. In each subsystem the solution obeys the Helmgoltz equation [115]

$$
-\nabla^2 \psi(x, y) = \frac{\omega^2}{c^2}\psi(x, y). \qquad (55)
$$

In what follows, all quantities are measured in terms of the light velocity c. This equation is completely equivalent to the case of electron transmission in a semiconductor, leading to

$$-\nabla^2\psi(x,y) = \frac{2m^*E}{\hbar^2}\psi(x,y),$$

where m^* is the effective electron mass with energy E. In the plane waveguides the solutions are given by TE propagating waves [137]

$$\psi_p(x,y) = \sqrt{\frac{1}{2\pi k_p}}\,\exp(\mathrm{i}k_p x)\phi_p(y) \tag{56}$$

$$\phi_p(y) = \sqrt{2}\,\sin(\pi p y) \tag{57}$$

with the eigenfrequency spectra

$$\omega^2 = k_p^2 + \pi^2 p^2, \quad p = 1,2,3,\ldots. \tag{58}$$

Here $\psi_p(x,y) = E_z(x,y)$ responds to the electric field component of EM field. The integer p numerates channels which are opened for increasing of the frequency as shown in figure 7. Other components of EM field can be easily expressed through $\psi(x,y)$ by use of the Maxwell equations [137]. The solutions inside the closed rectangular resonator are the following:

$$\psi_{mn}(x,y) = 2\sqrt{\frac{1}{L_xL_y}}\,\sin\left(\frac{\pi m x}{L_x}\right)\sin\left(\frac{\pi n y}{L_y}\right) \tag{59}$$

with the discrete eigenfrequencies

$$\omega_{m,n}^2 = \frac{\pi^2 m^2}{L_x^2} + \frac{\pi^2 n^2}{L_y^2} \tag{60}$$

where m and n are integers. Here and below, all dimensional quantities are measured in terms of the waveguide's width d, i.e. $d = 1$. These eigenfrequencies, dependent on the resonator width W, are shown in figure 8. With respect to the non-Hermitian effective Hamiltonian approach, it is important to note that the Helmgoltz equation (55) one by one is equivalent to the quantum mechanical description of the electron transmission through quantum dots with attached quantum wires. The squared frequency can be expressed as the quantum energy $E = \omega^2$ and the electric field directed perpendicular to metallic planes is equivalent to the quantum wave function [115] $E_z = \psi(x,y)$. However the effective non-Hermitian Hamiltonian (7) is to be modified with account of dispersion properties of microwave waveguides (58) as follows [111, 113]:

$$\mathcal{H}_{\mathrm{eff}} = \mathcal{H}_B - \mathrm{i}\sum_{C=\mathrm{L,R}}\sum_p W_{Cp}W_{Cp}^{\dagger}, \tag{61}$$

where the matrix elements of the coupling matrix elements between the m,nth eigenmode of the closed resonator and the pth propagation channel of the Cth waveguide equal

$$W_{mn;pC} = \sqrt{\frac{1}{\pi k_p}}\int_{-1/2}^{1/2}\mathrm{d}y\,\sin\left(\frac{\pi p y}{d}\right)\frac{\partial\psi_{mn}(x,y)}{\partial x}\bigg|_{x=x_C}, \tag{62}$$

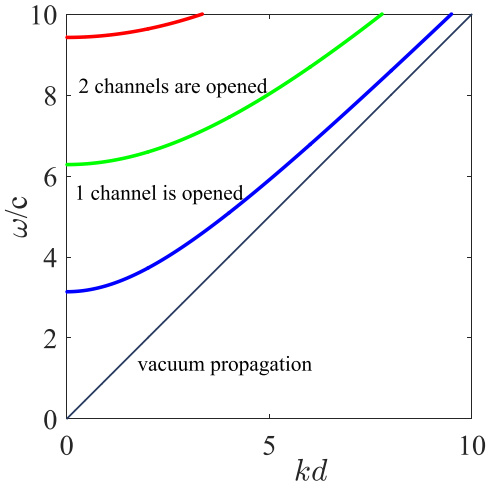

Figure 7. Dispersion curves of open channels in a planar waveguide with a rectangular cross-section.

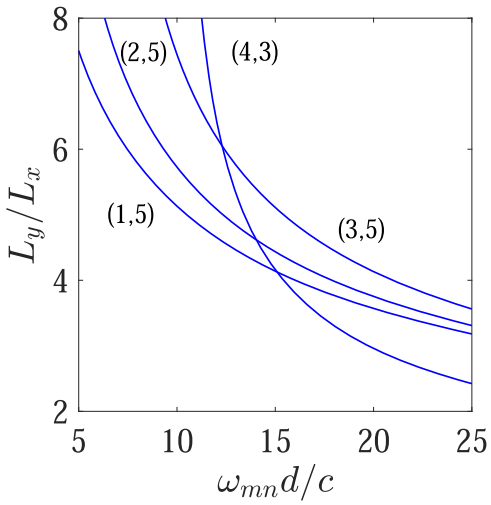

Figure 8. Selected frequencies (60) of the closed rectangular resonator vs width L_y. $E_0 = c^2/d^2$.

$C = \mathrm{L,R}$ enumerates the interfaces between the left and right waveguides shown in figure 1 by dashed lines $x_{\mathrm{L}} = -L_x/2, x_{\mathrm{R}} = L_x/2$. We note that the overlapping is given by derivatives of the eigenfunctions of the closed resonator over the transmission direction but not the eigenfunctions themselves, which equal zero at the boundaries shown in figure 1 by the dashed lines. In the present case of planar resonator, this is the x-direction as shown in figure 1. For the case of TM waves, the magnetic field $H_z(x,y)$ serves as the wave function $\psi(x,y)$ with the Neumann boundary conditions at the metallic walls of waveguide, which makes the problem fully equivalent to the transmittance of acoustic waves in a hard wall resonator. In that case, the form of the effective Hamiltonian remains the same but the coupling matrix elements takes the following form [112, 113]:

$$W_{mn;pC} = \sqrt{\frac{k_p}{\pi}}\int_{-1/2}^{1/2}\mathrm{d}y\,\sin\left(\frac{\pi p y}{d}\right)\psi_{mn}(x,y)\bigg|_{x=x_C}. \tag{63}$$

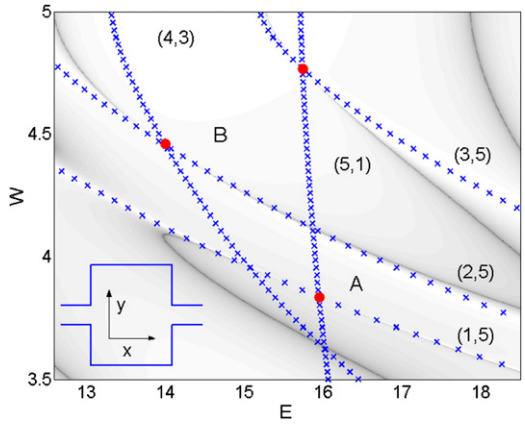

Figure 9. The transmittance in log scale through the rectangular resonator shown in the inset versus energy $E = \omega^2$ and width W of the resonator (in terms of the width of the lead). The dark areas correspond to low transmittance. The length of the resonator along the transport axis equals 4. The eigenfrequencies of the closed billiard are marked by times symbols (×). The positions of the BICs are shown by closed red circles. The patterns of the two BICs A and B are shown in figure 11. Reprinted figure with permission from [17], Copyright (2006) by the American Physical Society.

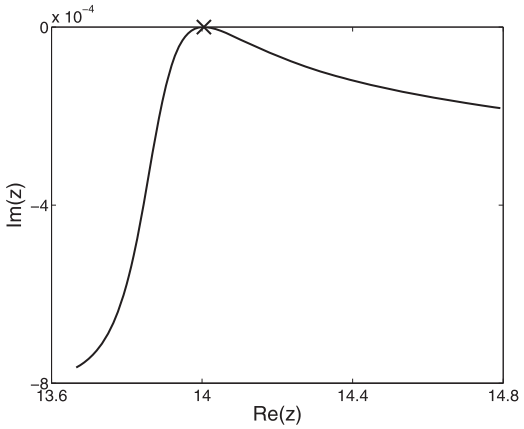

Figure 10. The evolution of resonance width Im(z) and position Re(z) of one of the two resonance states in the vicinity of the BIC B in figure 9. Im(z) vanishes at $L_y = 4.45$ (marked by an x). The widths of the other resonance states are much larger and are not shown here. Reprinted figure with permission from [17], Copyright (2006) by the American Physical Society.

The S-matrix is given by [108, 117]

$$S_{CC'} = \delta_{CC'} - 2\mathrm{i}\widehat{W}^C \frac{1}{E - \widehat{H}_{\mathrm{eff}}} \widehat{W}^{C'}. \tag{64}$$

In figure 9 we show the transmittance in the first open channel vs the incident frequency $E = \omega^2$ and the width of resonator W.

In the framework of this formalism, the positions and decay widths of the resonance states follow from the complex eigenvalues of the non-Hermitian effective Hamiltonian

$$\widehat{H}_{\mathrm{eff}}|\lambda) = z_\lambda|\lambda) \tag{65}$$

where $z_\lambda = E_\lambda - \mathrm{i}\gamma_\lambda/2$. The biorthogonal eigenstates are normalized as $(\lambda|\lambda') = \delta_{\lambda,\lambda'}$, where $(\lambda|$ is given by transpose of $|\lambda)$. Similar to the two-level approach for description of BICs in section 3 the BIC of the present formalism is given by those eigenstate of the effective Hamiltonian, whose eigenvalue is real. However as distinct of phenomenological case by Friedric and Wintgen [7] (see also [12]) the coupling matrix elements (63) are frequency dependent through equation (58). Then the resonant positions and widths are obtained by solving the corresponding fixed-point equations [109]

$$E_\lambda = \mathrm{Re}(z_\lambda(E_\lambda)), \qquad 2\gamma_\lambda = -\mathrm{Im}(z_\lambda(\gamma, E_\lambda)). \tag{66}$$

Moreover the rank of matrix of the effective Hamiltonian is defined by number of the eigenmodes of closed resonator whose number rigorously speaking is infinite. In order to solve the eigenvalue problem one has to decimate the matrix however a convergence of the matrix of the effective Hamiltonian is controversial for the Dirichlet BC [112]. In practice we explore the tight-binding approach for the effective Hamiltonian [111] which is equivalent to finite difference method of solution of the Helmholtz equation (55). The one half of eigenvalues of the effective non-Hermitian Hamiltonian (61) are real and correspond to the SP BICs because they are antisymmetric relative to $y \to -y$ and therefore have zero couplings (62) with the first channel continuum $p = 1$ provided that $\omega^2 < 4\pi^2$. The second half of the eigenvalues is complex and correspond to resonances for wave transmission through the rectangular resonator. However a very few of these complex eigenvalues have a tendency to acquire zero imaginary parts for variation of the width of the resonator at the vicinity of those points where a degeneracy of the eigenfrequencies (60). One of such events is shown in figure 10 where other eigenfrequencies are excluded in order to avoid obscure picture.

One can see from figure 9 that these BICs are located in very close vicinity to the points of degeneracy of the eigenmodes of the close resonator. Indeed when the eigenmodes, say ψ_1 , become degenerate one can superpose the eigenmodes as $\psi = a_1\psi_1 + a_2\psi_2$. Although each eigenmode is coupled with the continuum $|C\rangle$ via the coupling constants $W_1 = \langle C|\psi_1\rangle \neq 0$ and $W_2 = \langle C|\psi_2\rangle \neq 0$, the coupling of the superposed state $W = \langle C|\psi\rangle = a_1W_1 + a_2W_2$ can be canceled by a proper choice of the superposition coefficients a_1 and a_2 [17]. Then this state ψ becomes the BIC, which is decoupled from the waveguides for the case $E < 4\pi^2$.

The BIC function. In general case the scattering wave function obeys the following equation [111, 112]:

$$\begin{aligned}
\psi_{\mathrm{L}}(x,y) &= \frac{1}{\sqrt{4\pi k_1}}\left[\mathrm{e}^{\mathrm{i}k_1 x}\phi_1(y) + \sum_p S_{1L;pL}\,\mathrm{e}^{-\mathrm{i}k_p x}\phi_p(y)\right], \quad x < -L_x/2,\\
\psi_B(x,y) &= -\mathrm{i}\sum_{m'n'} G_{mn;m'n'}\sqrt{\frac{k_{p=1}}{\pi}}W_{m'n';1L}\psi_{m'n'}(x,y), \quad -L_x/2 < x < L_x/2,\\
\psi_{\mathrm{R}}(x,y) &= \sum_p \frac{1}{\sqrt{4\pi k_p}} S_{1L;p\mathrm{R}}\,\mathrm{e}^{\mathrm{i}k_p x}\phi_p(y), \quad x > L_x/2,
\end{aligned} \tag{67}$$

where $S_{pC,p'C'}$ are components of the S-matrix (64) and the Green function $\hat{G}$ is the inverse of the matrix $\omega^2 - \widehat{H}_{\mathrm{eff}}$. So,

inside the resonator the wave function is given by the Lippmann–Schwinger equation [111, 112]:

$$(\omega^2 - \widehat{H}_{\text{eff}})|\psi_B\rangle = \widehat{W}_{Lp=1} a^*_{L,p=1}|L, p=1\rangle, \tag{68}$$

where the waveguide states are given by the incoming wave amplitude $a^+_{L,p=1}$ for the present case of 2D wave transmission shown in the inset of figure 9. We imply that the wave enters through the left waveguide. Equation (68) has an unambiguous solution until the operator at the left can be inverted. However, if

$$\|\omega^2 - \widehat{H}_{\text{eff}}\| = 0, \tag{69}$$

the inverse operator does not exist, and the solution becomes ambiguous.

Such a precedent was revealed in a periodical structure (grating slab) [138] and is a consequence of bound states in the diffraction continuum [31, 32]. If equation (69) is fulfilled, then the solution of equation (68) can be presented as superposition [133]

$$|\psi_B\rangle = \alpha|\text{BIC}\rangle + |\psi_p\rangle, \tag{70}$$

where the first part is the solution of the homogeneous equation

$$(\omega^2 - \widehat{H}_{\text{eff}})|\text{BIC}\rangle = 0, \tag{71}$$

while the second contribution is the particular solution of equation (68). In the presentation of eigenstates (65) equation (69) takes the following form:

$$\prod_{\lambda}(\omega^2 - z_\lambda) = 0. \tag{72}$$

Obviously, equation (69) is fulfilled if some of complex eigenvalues become real, i.e. at the BIC point. Then, the necessary and sufficient condition for existence of solution of the equation (68) is that the vector [133]

$$\langle\text{BIC}|\psi_p\rangle = 0. \tag{73}$$

This equation has the clear physical meaning that the BIC solution is orthogonal to the solution which propagates in waveguide, and therefore cannot leakfrom the cavity.

It might seem that the BIC solution (47) can be presented by only those eigenfunctions (59) which undergo degeneracy, events of which are shown in figure 8. In particular, let us consider the eigenmodes $\psi_{4,3}$ and $\psi_{2,5}$ with corresponding eigenfrequencies

$$\begin{aligned}\omega^2_{4,3} &= \omega^2_a = \frac{4^2}{L_x^2} + \frac{3^2}{L_y^2},\\ \omega^2_{2,5} &= \omega^2_b = \frac{2^2}{L_x^2} + \frac{5^2}{L_y^2}.\end{aligned} \tag{74}$$

All dimensional units are measured in term of the waveguide width d, and frequency is measured in term of $\sqrt{E_0} = \frac{c}{d}$. The degeneracy point is given by relation $\frac{L_y}{L_x} = \frac{2}{\sqrt{3}}$ and respectively the BIC frequency equals $\omega_c = \frac{4\pi}{L_x}\sqrt{1 + \frac{27}{64}}$. In numerics we have chosen $L_x = 4$ that gives $\omega_c = 3.746$. Then the coupling matrix elements (62) equal

$$\begin{aligned}W_{4,3;1\text{L}} = W_{4,3;1\text{R}} = W_a = \sqrt{\frac{2}{k_1}}\frac{8\pi}{L_x^{3/2}L_y^{1/2}}\\ \times \int_{-1/2}^{1/2} \text{d}y\, \cos(\pi y)\cos(3\pi y/L_y) \approx 0.618,\end{aligned}$$

$$\begin{aligned}W_{2,5,1\text{L}} = W_{2,5;1\text{R}} = W_b = \sqrt{\frac{2}{k_1}}\frac{4\pi}{L_x^{3/2}L_y^{1/2}}\\ \times \int_{-1/2}^{1/2} \text{d}y\, \cos(\pi y)\cos(5\pi y/L_y) \approx 0.4.\end{aligned}$$

Thus, the BIC solution in a two-level approximation can be written as the linear superposition, at least, at the point of degeneracy $\omega = \omega_c$,

$$\psi_{\text{BIC}}(x, y) = \psi_0(W_b\psi_a(x, y) - W_a\psi_b(x, y)), \tag{75}$$

where indices 4, 3 and 2, 5 are absorbed by the indices a and b respectively. One can easily verify that this function is orthogonal to the first continuum of both waveguides given by $p = 1$ and turns to zero at the boundaries $x = \pm L_x/2$, and therefore is localized inside the resonator. The matrix of the effective Hamiltonian (61) takes the following form:

$$\begin{pmatrix} \omega_1^2 - 2\text{i}W_1^2 & -2\text{i}W_1W_2 & \dots & -2\text{i}W_1W_a & -2\text{i}W_1W_b \\ -2\text{i}W_1W_2 & \omega_2^2 - 2\text{i}W_2^2 & \dots & -2\text{i}W_2W_a & -2\text{i}W_2W_b \\ \vdots & \vdots & \ddots & \vdots & \vdots \\ -2\text{i}W_1W_a & -2\text{i}W_2W_a & \dots & \omega_a^2 - 2\text{i}W_a^2 & -2\text{i}W_aW_b \\ -2\text{i}W_1W_b & -2\text{i}W_2W_b & \dots & -2\text{i}W_b^2 & \omega_b^2 - 2\text{i}W_aW_b \end{pmatrix} = 0. \tag{76}$$

The equation for the BIC takes the following form:

$$\begin{vmatrix} \frac{\omega_1^2 - \omega^2}{2\text{i}W_1^2} + 1 & 1 & \dots & 1 & 1 \\ 1 & \frac{\omega_2^2 - \omega^2}{2\text{i}W_2^2} & \dots & 1 & 1 \\ \vdots & \vdots & \ddots & \vdots & \vdots \\ 1 & 1 & \dots & \frac{\omega_a^2 - \omega^2}{2\text{i}W_a^2} & 1 \\ 1 & 1 & \dots & 1 & \frac{\omega_b^2 - \omega^2}{2\text{i}W_b^2} \end{vmatrix}. \tag{77}$$

One can see that at the points of degeneracy $\omega_a = \omega_b$ and $\omega = \omega_a$, the determinant (77) turns to zero to realize the BIC as the linear superposition of degenerate states (75).

What is the role of the evanescent modes? First, we show that the evanescent modes shift the BIC point. The effective Hamiltonian (61) can be rewritten as follows for $\omega^2 < 4\pi^2$:

$$\widehat{H}_{\text{eff}} = \widehat{\widetilde{H}}_B - 2\text{i}\widehat{W}_1\widehat{W}_1^\dagger, \tag{78}$$

where

$$\widehat{\widetilde{H}}_B = \widehat{H}_B - 2\sum_{p>1}\widehat{\widetilde{W}}_p\widehat{\widetilde{W}}_p^\dagger, \tag{79}$$

where the coupling matrix $\widehat{W}_{p=1}$ is defined by equation (62) or equation (63) while the coupling matrix $\widehat{\widetilde{W}}_{p>1}$ originated from the evanescent modes and equals

$$\widetilde{W}_{mn;p>1} = \sqrt{\frac{1}{\pi|k_p|}} \int_{-1/2}^{1/2} \mathrm{d}y \, \sin \times \left(\frac{\pi p y}{d}\right) \frac{\partial \psi_{mn}(x,y)}{\partial x}\bigg|_{x=\pm L_x/2}. \quad (80)$$

The factor 2 in equations (78) and (79) is the result of equal contribution of both the left and right waveguides. The matrix $\widehat{\widetilde{H}}_B$ is Hermitian and can be interpreted as the effective Hamiltonian of the cavity modified by evanescent modes. Substituting modified eigenvalues into (77) we obtain that their points of degeneracy define the exact BIC points.

Second, the approximate BIC solution (75) turns to zero at the boundaries between the resonator and waveguides $x = \pm L_x/2$. The exact BIC solution is defined by equation (71), which can be expressed in series of the eigenfunctions of the closed resonator

$$\psi_{\mathrm{BIC}}(x,y) = \sum_{mn} a_{mn}\psi_{mn}(x,y), \quad (81)$$

where the expansion coefficients are given by the eigenvector of equation (71). Although each eigenfunction ψ_{mn} $(x = \pm L_x/2, |y| < 1/2) = 0$, the BIC solution (81) is to be sewed with the evanescent modes in the waveguides, which exponentially decay when we move away from the boundary of the closed resonator:

$$\sum_{mn} a_{mn}\psi_{mn}(x = \pm L/2, |y| < 1/2) = \sum_{p>1} \frac{a_p}{\sqrt{4\pi k_p}}\phi_p(y) \approx \frac{a_2}{\sqrt{4\pi k_2}}\phi_2(y). \quad (82)$$

We note that if restricted by only two eigenfunctions which undergo degeneracy in the vicinity of the BIC point, the left hand expression in equation (82) would turn to zero. Only due to the infinite series over the eigenfunctions does the left hand expression (82) differ from zero. Thus, the second role of the evanescent modes is in the exponential weak blowing of the BIC solution into waveguides that provides smooth behavior of the BIC solution, as seen from figure 11. These BIC solutions are found numerically from equation (71) with a sufficiently large rank of the effective Hamiltonian. Thus, there are two important features of the BICs caused by evanescent modes. First, the BIC solution is overflowed from the resonator due to coupling to the evanescent modes, as seen from figure 11. A degree of the overflowing is given by the exponential contribution of the first evanescent mode $\exp(-\sqrt{(2\pi)^2 - \omega^2}$ $(x - L_x/2))$ in the right waveguide. The same holds in the left waveguide, however for $x < -L/2$. Second, the BIC point is shifted relative to the points of degeneracy of the eigenmodes of the closed resonator because of the contribution in the effective Hamiltonian (79). The details of these effect will be given below for the 3D resonators, where the contribution of evanescent modes has principal importance for existence of BICs.

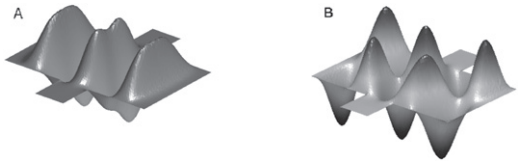

Figure 11. The patterns of the two BICs A and B marked in figure 9 by bold circles. Reprinted figure with permission from [17], Copyright (2006) by the American Physical Society.

7. Accidental BICs in the Sinai shaped open cavity

The rectangular cavity is an example of an integrable system where the variables x and y are separated that reduces the eigenvalue problem to a one-dimensional one with multiplicative eigenfunctions (59). Thus, for the variation of one of the scales of the resonator, say width W, we have multiple events of degeneracy, each of which gives rise to the BICs in the Friedrich–Wintgen scenario, as described in previous section. In fact there are only a few integrable resonators and elliptic and equilateral triangles which are specified by the Poisson distribution of the nearest distances between the eigenlevels. All the rest are considered non-integrable, whose eigenlevels undergo avoided crossings for the variation of some parameter with the Wigner distribution and form so-called chaotic billiards [115]. The Bunimovich and Sinai billiards are well-known examples of chaotic billiards. Experimentally it is easy to transform the integrable billiard into a chaotic one by embedding a dielectric or metallic disk inside the plane rectangular cavity as sketched in figure 12. Then the FW mechanism of the BIC due to the degeneracy of the eigenstates of the closed billiard is not applicable. However there is another way to realize the BIC, by decoupling an individual eigenmode of the Sinai billiard from the first continuum of the waveguides [50, 55]. For that we smoothly deform the eigenmodes by, for example, variation of the radius or the position of the disk inserted inside the rectangular cavity. The effect of disk can be described by a circular potential perturbation

$$V(x,y) = V_g \exp\left[-\frac{(x-x_0)^2 + (y-y_0)^2}{\mathrm{R}^2}\right] \quad (83)$$

added into the effective Hamiltonian (61). To be specific, we consider the Neumann boundary conditions because of the good convergence of the results with the growth of rank of the matrix $\widehat{H}_{\mathrm{eff}}$ for low lying eigenfrequencies [112].

In what follows we fix the radius $R = 1.5$ and position of circular potential at $x_0 = 0, y_0 = 1$ in terms of the waveguides' width d and vary the height V_g of the potential (83) that effectively varies the radius of the circular potential. Because of the symmetry of the full system relative to $x \to -x$ the continua of both waveguides are identical. Respectively we have identical coupling matrix elements of the Sinai resonator with

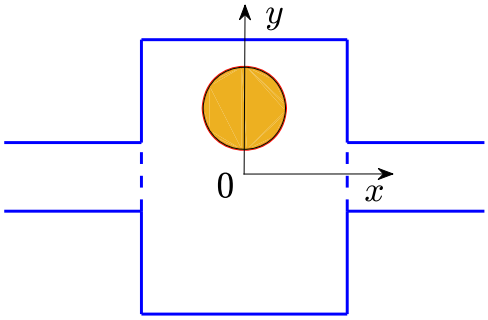

Figure 12. Dielectric or metallic disk inside the rectangular open resonator.

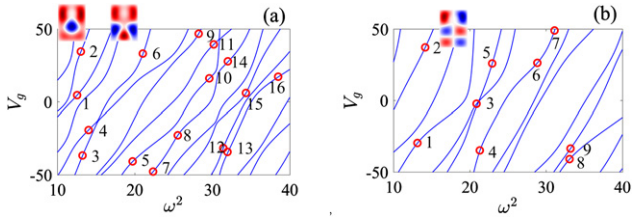

Figure 13. Eigenvalues and eigenfunctions of the soft Sinai resonator vs height of the potential (83). Insets show a few patterns of corresponding eigenfunctions even (a) and odd (b) relative to $x \to -x$. Open circles mark the BIC points. Reprinted from [29], Copyright (2017), with permission from Elsevier.

waveguide continua

$$W_{b,pC} = \sqrt{\frac{1}{k_p}} \int_0^d \mathrm{d}y \phi_p(y) \frac{\partial \psi_b(x,y)}{\partial x}\bigg|_{x=\pm L/2}, \qquad (84)$$

where $C = \mathrm{L}, \mathrm{R}$ enumerates the interfaces between the left and right waveguides shown in figure 12 by dashed lines, and ψ_b are the eigenfunctions of the closed Sinai billiard.

The eigenfunctions are classified as even and odd $\psi(x,y) = \pm\psi(-x,y)$. Respectively, the eigenvalues in each irreducible representation undergo avoided crossings with variation of V_g as illustrated in figure 13. For clarity we show some patterns of the eigenfunctions at $V_g = 50$ in figure 13. One can see that the eigenfunctions are depleted inside by the potential (83) at $V_g = 50$. A variation of another parameter of the potential (83), for example, the radius or position, gives a similar result. Thus, we have no degeneracy of the eigenfunctions of the same irreducible representation in the chaotic Sinai resonator.

Figure 14 shows the transmittance calculated via equation (64). In order for the reader to observe that peaks of the transmittance follow the eigenvalues of the closed Sinai resonator, we reduce the coupling between the waveguides and the resonator by implementation of diaphragms between the waveguides and the billiard [139] that narrows transmission peaks. The BIC occurs if the resonance width turns to zero, given by the imaginary part of the complex eigenvalues of the effective non-Hermitian Hamiltonian

$$\widehat{H}_{\mathrm{eff}} = \widehat{H}_B + V_g - \mathrm{i} \sum_{C=\mathrm{L,R}} \sum_p \widehat{W}_{C,p} \widehat{W}^{\dagger}_{C,p}, \qquad (85)$$

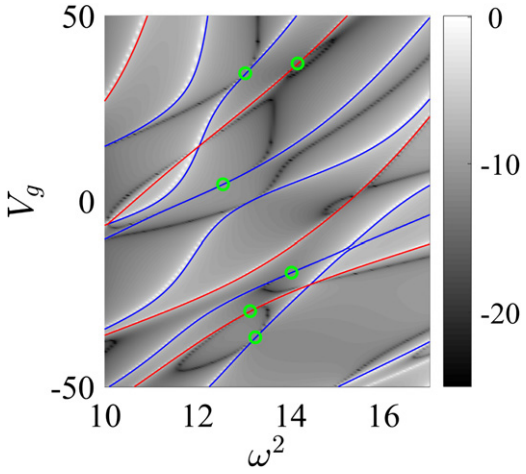

Figure 14. Transmittance of the Sinai resonator in log scale vs V_g (effective radius of the circular hole shown in figure 12) and incident frequency. The BICs are shown by open circles. Reprinted from [29], Copyright (2017), with permission from Elsevier.

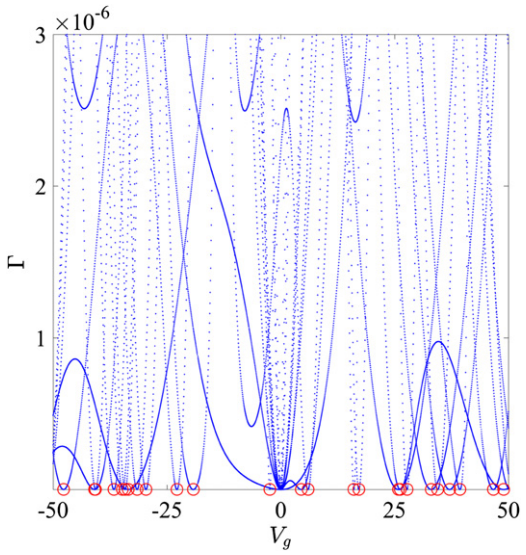

Figure 15. Evolution of the resonant widths for variation of the potential. Red open circles mark BICs. Reprinted from [29], Copyright (2017), with permission from Elsevier.

where $\widehat{\mathcal{H}}_B$ is the Hamiltonian of the closed rectangular resonator, and $\widehat{W}_{C,p}$ are columns of matrix elements (84) labeled by the eigenstate indices b. The numerically computed evolution of the resonant widths is presented in figure 15, which shows multiple events of the resonant widths turning to zero, i.e. BICs in the Sinai resonator. The even BICs sorted by their energies are shown in figure 13(a) by open circles. Respectively, the odd BICs are shown in figure 13(b). Besides these BICs, one can see in figure 15 numerous SP BICs at the point $V_g = 0$, which are the eigenfunctions of the rectangular resonator antisymmetric relative to $y \to -y$ for $\omega < 2\pi$. Therefore, they are incompatible with the symmetric propagating mode in the first channel $p = 1$ (57).

Figure 14 clearly demonstrates that the BIC points are positioned at those points in the parametric space of E and V_g

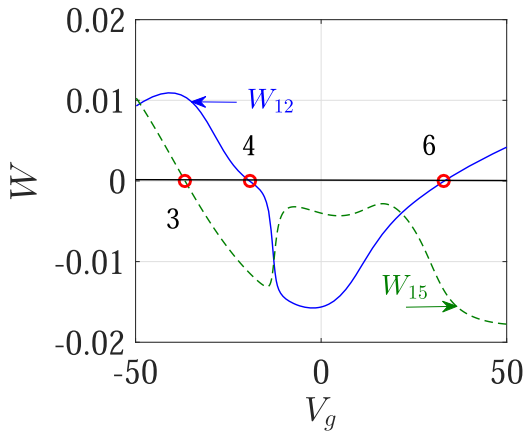

Figure 16. Evolution of the coupling matrix element (84) with V_g. Reprinted from [29], Copyright (2017), with permission from Elsevier.

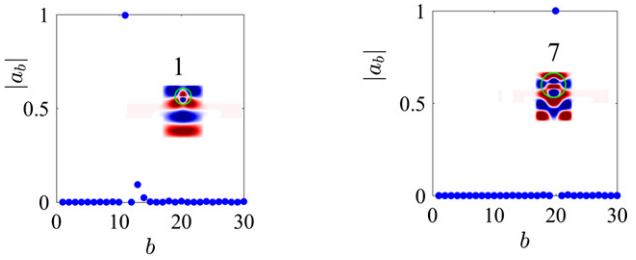

Figure 17. Patterns of even BICs enumerated according to table 2 with coefficients of the modal expansions. Position of potential (83) is shown in green circles.

where the transmission zero coalesces with the transmission unit, similar to the FW BICs [17] and illustrating the collapse of the Fano resonance [34]. However, in the Sinai billiard, the BICs occur accidentally under variation of the circular potential (83) that changes the eigenfunctions of the closed Sinai resonator as shown in the insets in figure 13. That in turn changes the coupling matrix elements (84) so that some of them can turn to zero as illustrated in figure 16. This is the mechanism of the accidental BICs patterns shown in figures 17 and 18. These figures also depict the modal expansion coefficients $|a_b|$ of BICs over the eigenmodes of the closed Sinai resonator

$$\psi_{\rm BIC}(x,y)=\sum_b a_b\psi_b(x,y). \tag{86}$$

One can see that indeed basically one eigenfunction contributes into the BIC mode. There is also a background of other eigenfunctions, which is the result of thecontribution of evanescent modes into the effective Hamiltonian (see discussion in previous section).

In what follows we will prove that if one of the coupling matrix elements $W_{b,p=1}$ vanishes, then the accidental BIC occurs embedded into the continuum of the first propagating channel $p=1$ of both waveguides $C=\mathrm{L},\mathrm{R}$. Let us choose, for example, the eigenfunction of the closed billiard, say $b=3$, whose coupling with the first channel $p=1$ turns to zero. Then we can write the coupling matrix (84) as follows:

$$W_{b,1}=(W_1\ W_2\ 0\ W_4\ \ldots). \tag{87}$$

Table 2. BICs even relative to $x\to -x$ marked by open circles in figure 13(a). Reprinted from [29], Copyright (2017), with permission from Elsevier.

Number of the even BIC	E	V_g
1	12.550	4.5
2	13.029	34.45
3	13.244	−36.65
4	14.026	−19.2
5	19.709	−40.7
6	21.025	33.05
7	22.355	−47.7
8	25.541	−22.8
9	28.236	46.7
10	29.608	16.05
11	30.181	39.35
12	31.418	−31.55
13	31.960	−34.2
14	32.002	27.75
15	34.333	6.00
16	38.495	17.15

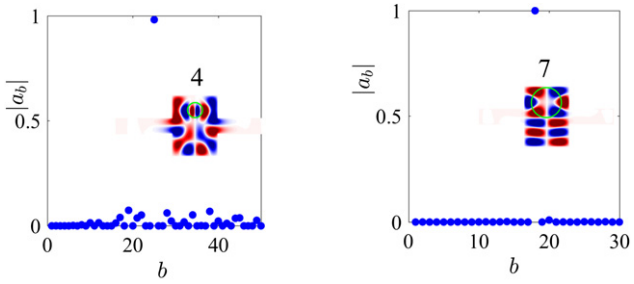

Figure 18. Patterns of odd BICs enumerated according to table 3 with coefficients of the modal expansions.

Table 3. BICs odd relative to $x\to -x$ marked by open circles in figure 13(b).

Number of the odd BIC	E	V_g
1	13.133	−29.6
2	14.155	37.1
3	20.882	−2.4
4	21.307	−34.8
5	22.927	25.85
6	28.844	26.25
7	31.099	48.95
8	33.063	−40.9
9	33.189	−33.5

Because of symmetry relative $x\to -x$, the coupling matrix (87) is invariant relative to choice of waveguides $C=\mathrm{L},\mathrm{R}$. Then there is a vector

$$\psi_3^+=(0\ 0\ 1\ 0\ \ldots), \tag{88}$$

which is the eigen null vector of the matrix $WW^+\psi_3=0$. On the other hand, the vector (88) is the eigenvector of the closed

billiard with the Hamiltonian

$$\widehat{H}_B = \begin{pmatrix} \omega_1^2 & 0 & 0 & 0 & \dots \\ 0 & \omega_2^2 & 0 & 0 & \dots \\ 0 & 0 & \omega_3^2 & 0 & \dots \\ 0 & 0 & 0 & \omega_4^4 & \dots \\ \vdots & \vdots & \vdots & \ddots & \end{pmatrix} \tag{89}$$

with the eigenfrequency ω_3. Thus the null eigenvector (88) is the eigenstate of the effective non-Hermitian Hamiltonian (85) with the real eigenfrequency ω_3, and therefore is the BIC with this frequency. This result does not depend on the other coupling matrix elements in (87). Following references [31, 32], we define such BICs as accidental. Note that this conclusion is correct in neglecting the evanescent modes of waveguides. The contribution of evanescent modes can be performed as in section 6. However in this case, the eigenstate (88) ceases to be the eigenstate of the effective Hamiltonian. As a result, as figure 18(a) shows, the accidental BIC blows off the Sinai billiard and modal expansion shows a noticeable background of all other eigenmodes of the billiard.

8. The cylindrical resonator with non-axisymmetric waveguides. The twisted BICs

The aim of this section and those that follow is to demonstrate the nontrivial role of the waveguides whose attachment breaks the symmetry of the closed resonators with nontrivial BICs embedded into continua of these waveguides. For example, the closed cylindrical resonator with radius R and length L is a typical textbook case [137] that allows separation of variables in the cylindrical system of coordinates. If one attaches cylindrical waveguides coaxially as shown in figure 19(a), the axial symmetry of the total open system is preserved. We skip this case of coaxially connected waveguides where the FW BICs are accessed via the variation of the length of the resonator L [140], similar to section 6 (planar rectangular resonators). However if one of the waveguides is shifted off the symmetry axis of the resonator as shown in figure 19(b), the axial symmetry of the total system breaks. We consider the case of non-axisymmetric waveguides which are identical but are attached to the resonator by different angles so that the waveguides are unwrapped by angular difference $\Delta\phi$ as shown in figure 19. This does not change the strength of the coupling matrix elements with continua but differs the continua by phase. We show that, nevertheless, the BICs exist but have to be twisted by the angle $\Delta\phi$.

The Helmholz equation (55) can be applied for acoustic transmission through duct–cavity structures in a hard wall approximation. The equation takes the following form in the cylindrical system of coordinates:

$$\left[\frac{\partial^2}{\partial r^2} + \frac{1}{r}\frac{\partial}{\partial r} - \frac{m^2}{r^2} + \frac{\partial^2}{\partial z^2} + \omega^2\right]\psi = 0, \tag{90}$$

for the non-dimensional velocity potential ψ where the non-dimensional coordinates r and z are normalized by the waveguide radius r_w. The dimensionless frequency ω is defined through the dimensional frequency $\widetilde{\omega}$ as follows $\omega = \widetilde{\omega} r_w / c_0$ and c_0 is the sound speed.

Figure 19. Cylindrical resonator with (a) a coaxially and (b) a non-coaxially attached non-axisymmetric cylindrical waveguide. The input waveguide can freely move along the resonator axis and rotate about the symmetry axis of the resonator. Reprinted from [141], Copyright (2018), with permission from Elsevier.

The propagating modes in the sound hard cylindrical waveguides with Neumann boundary conditions are described by

$$\psi_{pq}(\rho, \alpha, z) = \psi_{pq}(\rho)\frac{1}{\sqrt{2\pi k_{pq}}}\exp(\mathrm{i}p\alpha + \mathrm{i}k_{pq}z), \tag{91}$$

$$\psi_{pq}(\rho) = \begin{cases} \dfrac{\sqrt{2}}{J_0(\mu_{0q})}J_0(\mu_{0q}\rho), & p = 0, \\ \sqrt{\dfrac{2}{\mu_{pq}^2 - p^2}}\dfrac{\mu_{pq}}{J_p(\mu_{pq})}J_p(\mu_{pq}\rho), & p = 1, 2, 3, \dots, \end{cases}$$

where ρ, α are the polar coordinates shown in figure 20, μ_{pq} is the qth root of equation

$$\left.\frac{\mathrm{d}J_p(\mu_{pq}\rho)}{\mathrm{d}\rho}\right|_{\rho=1} = 0$$

imposed by the Neumann boundary condition on the walls of sound hard cylindrical waveguide:

$$k_{pq}^2 = \omega^2 - \mu_{pq}^2. \tag{92}$$

The dimensional quantities ρ, z, k_{pq} are measured in terms of the radius of the waveguide ρ, and the frequency is measured in the terms of the ratio s/ρ, where s is the sound velocity. The propagating bands degenerate with respect to the sign of azimuthal index and are classified by two indices, the azimuthal index $p = 0, \pm1, \pm2, \dots$ and radial index $q = 1, 2, 3, \dots$. Profiles of the propagating functions $\psi_{pq}(\rho)\cos p\alpha$ are depicted in table 4.

The Hilbert space of the closed cylindrical resonator is given by the following eigenmodes:

$$\Psi_{mnl}(r, \phi, z) = \psi_{mn}(r)\sqrt{\frac{1}{2\pi}}\exp(\mathrm{i}m\phi)\psi_l(z), \tag{93}$$

where

$$\psi_{mn}(r) = \begin{cases} \dfrac{\sqrt{2}}{RJ_0(\mu_{0n}R)}J_0\left(\dfrac{\mu_{0n}r}{R}\right), & m = 0 \\ \sqrt{\dfrac{2}{\mu_{mn}^2 - m^2}}\dfrac{\mu_{mn}}{RJ_m(\mu_{mn}R)}J_m\left(\dfrac{\mu_{mn}r}{R}\right), & m = 1, 2, 3, \dots, \end{cases}$$

$$\psi_l(z) = \sqrt{\frac{2 - \delta_{l,1}}{L}}\cos[\pi(l-1)z/L], \tag{94}$$

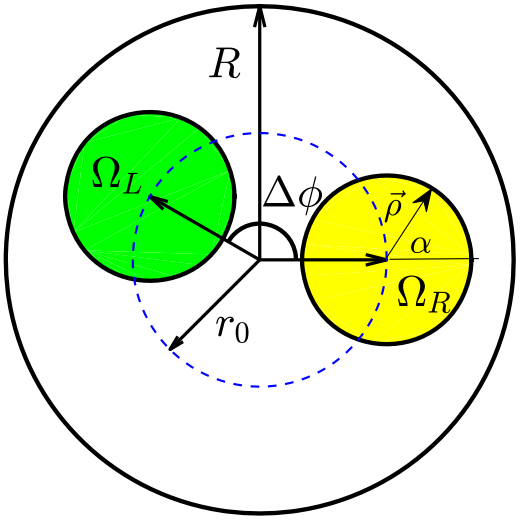

Figure 20. Filled areas show the overlapping integration area in the coupling matrix (96). Reprinted from [141], Copyright (2018), with permission from Elsevier.

Table 4. Cut-off frequencies and corresponding shapes of the propagating modes in the circular waveguide.

Channel	Cut-off frequency	Indices	Mode shape
1	0	$p = 0, q = 1$	
2	1.841 18	$p = \pm 1, q = 1$	
3	3.0542	$p = \pm 2, q = 1$	
4	3.831 706	$p = 0, q = 2$	

$l = 1, 2, 3, \ldots$ and z are measured in terms of the waveguide radius. The corresponding eigenfrequencies are

$$\omega^2_{mnl} = \left[\frac{\mu^2_{mn}}{R^2} + \frac{\pi^2(l-1)^2}{L^2}\right], \tag{95}$$

where μ_{mn} is the nth root of the equation $\frac{\mathrm{d}J_m(\mu_{mn}r)}{\mathrm{d}r}\big|_{r=R} = 0$ which follows from the Neumann BC on the walls of hard cylindrical resonator.

The matrix elements of $\widehat{W}$ are given by overlapping integrals [112, 141]:

$$\begin{aligned} W^C_{mnl;pq} &= \int_{\Omega_C} \rho\,\mathrm{d}\rho\,\mathrm{d}\alpha\psi_{pq}(\rho,\alpha)\Psi^*_{mnl}(r,\phi,z=z_C) \\ &= \int_0^{2\pi}\mathrm{d}\alpha\int_0^1 \rho\,\mathrm{d}\rho\,\psi_{pq}(\rho,\alpha)\Psi^*_{mnl} \\ &\quad\times(r(\rho,\alpha),\phi(\rho,\alpha),z_C) \\ &= \psi_l(z_C)\int_0^{2\pi}\mathrm{d}\alpha\int_0^1\rho\,\mathrm{d}\rho\psi_{pq}(\rho,\alpha)\psi^*_{mn} \\ &\quad\times(r(\rho,\alpha),\phi(\rho,\alpha)), \end{aligned} \tag{96}$$

where $\Omega_{C,C=\mathrm{L,R}}$ are the interfaces positioned at $z_C = 0, L$. Integration is performed over a circular cross section of the attached waveguides as shown in figure 20. One can link the polar coordinates of the resonator with that of the immovable waveguide

$$r\,\sin\,\phi = \rho\,\sin\,\alpha, \qquad r\,\cos\,\phi = r_0 + \rho\,\cos\,\alpha,$$

where r_0 is the distance between the axes of the waveguide and resonator.

According to equation (93) we have

$$\psi_l(z=0) = \sqrt{\frac{2-\delta_{l,1}}{L}}, \qquad \psi_l(z=L) = \psi_l(0)(-1)^{l-1}. \tag{97}$$

Substituting (97) into (96) we obtain the following relation between the left and right coupling matrix elements:

$$W^{\mathrm{L}}_{mnl;pq} = (-1)^{l-1}\,\mathrm{e}^{\mathrm{i}(p-m)\Delta\phi}W^{\mathrm{R}}_{mnl;pq}. \tag{98}$$

Therefore the matrix of the effective Hamiltonian takes the following form:

$$\begin{aligned} \langle mnl|\widehat{H}_{\mathrm{eff}}|m'n'l'\rangle &= \omega^2_{mnl}\delta_{mm'}\delta_{nn'}\delta_{ll'} \\ &\quad -\mathrm{i}\sum_{pq}k_{pq}[1+(-1)^{l+l'}\,\mathrm{e}^{\mathrm{i}(m'-m)\Delta\phi}] \\ &\quad\times W_{mnl;pq}W^*_{m'n'l';pq}. \end{aligned} \tag{99}$$

The transmittance of sound waves in the p, q propagating channel through the resonator is given by the following equation [112]:

$$\begin{aligned} T_{pq;pq} &= 2\mathrm{i}k_{pq}\sum_{mnl}\sum_{m'n'l'}W_{mnl;pq}\,\mathrm{e}^{-\mathrm{i}m'\Delta\phi} \\ &\quad\times G_{mnl;m'n'l'}W^*_{m'n'l';p'q'}, \end{aligned} \tag{100}$$

where

$$\hat{G} = \frac{1}{\omega^2 - \widehat{H}_{\mathrm{eff}}}, \tag{101}$$

that is, the propagation of waves through the resonator is described by the Green function which is inverse of the matrix $\omega^2 - \widehat{H}_{\mathrm{eff}}$ and coupling matrices of the resonator with the input (left) waveguide and the output (right) waveguide. However, the most noteworthy feature in equation (100) is the complex phases of the coupling matrix elements between states the with different azimuthal indices, m and p. As we show below this drastically changes the transmittance.

8.1. Variation over the length of resonator at $\Delta\phi = \pi/4$

The case of $\Delta\phi \neq 0$ is interesting in that we are faced with the problem of embedding the BIC into two continua which differ in their phases. First, the problem of the BIC residing in a finite number of continua was considered by Pavlov-Verevkin and coauthors [142]. A rigorous statement about the BICs was formulated as follows. The interference among N degenerate states which decay into K non-interacting continua generally leads to the formation of $N - K$ BICs. The equivalent point of view [17] is that the linear superposition of the N degenerate eigenstates $\sum_{n=1}^{N} a_n\psi_n$ can be adjusted to have zero coupling with K different continua in $N - K$ ways by

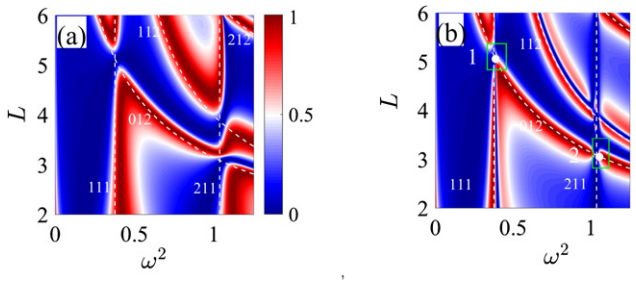

Figure 21. Transmittance of a cylindrical resonator vs frequency and length of the resonator L at (a) $\Delta\phi = 0$ and (b) $\Delta\phi = \pi/4$. Dashed lines show eigenlevels of the closed resonator with corresponding indices mnl. The positions of the BICs are shown by closed circles. Reprinted from [141], Copyright (2018), with permission from Elsevier.

variation of the N superposition coefficients a_n. Respectively, that involves K-parametric avoiding crossing. The number of continua can grow due to a number of reasons, for example, non-symmetrically attached waveguides, multiple propagation subbands in the waveguides, or two polarizations of the radiation continuum in case of EM BICs. Each case puts the problem of searching for BICs embedding into many continua on the edge of art [31, 55, 59, 143–145].

In what follows we take both waveguides with the unit radius shifted relative to the central axis of the resonator with radius $R = 3$ by a distance $r_0 = 1.5$. We consider transmission in the first channel $p = 0, q = 1$ in the frequency domain $0 < \omega < \mu_{11} = 1.8412$ (see table 2). Although rotation of the waveguide does not alter its propagating modes (continua), it provides the complex phases in the coupling matrix elements of the resonator eigenmodes with the continua as given by equation (98). That effects the transmittance as shown in figure 21.

As before, the BIC points are detected by finding a zero resonant width for variation of the resonator's length L at fixed $\Delta\phi = \pi/4$ as shown in figure 22. We marked in circles only those BICs which are listed in table 5 and will be analyzed below. The positions of the BICs and expansions coefficients over the eigenmodes of closed resonator (93)

$$\psi_{\rm BIC}(r,\phi,z) = \sum_{mnl} a_{mnl}\Psi_{mnl}(r,\phi,z) \qquad (102)$$

are collected in table 5. Figure 23 shows the third and fourth BICs marked in figure 21(b), which are the eigenmodes of the non-Hermitian effective Hamiltonian (99). Figure 23 clearly shows that the BICs at $\Delta\phi \neq 0$ are decoupled from the first channel owing to twisting of the BIC modes by the rotation angle $\Delta\phi$.

8.2. Arbitrary $\Delta\phi$. Wave faucet

Equation (100) shows that the phase difference $\Delta\phi$ due to the rotation of the input waveguide brings an important contribution into the interference between resonances. Figure 24 vividly illustrates the high sensitivity of the transmittance to the rotation angle $\Delta\phi$. As seen from figure 21 the eigenmode 012 crosses the eigenmodes ± 111 around $L = 5$. Respectively, the transmittance is basically given by the interference of these

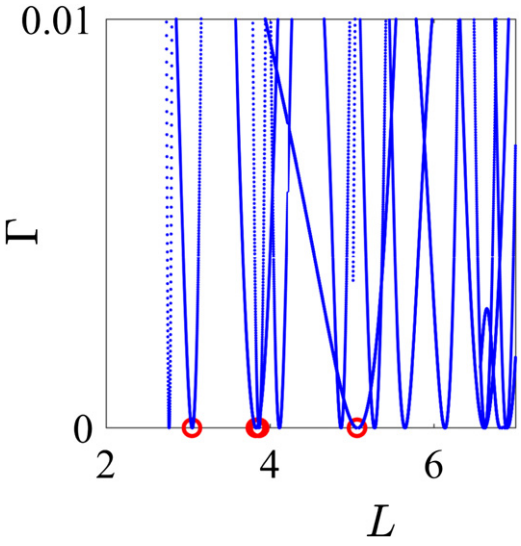

Figure 22. Evolution of resonant widths under the variation of the resonator length at $\Delta\phi = \pi/4$. Circles mark BICs listed in table 3. Reprinted from [141], Copyright (2018), with permission from Elsevier.

Table 5. BICs at $\Delta\phi = \pi/4$. The waveguides with the unit radius are shifted relative to the axis of cylindrical resonator with radius $R = 3$ by a distance $r_0 = 1.5$.

BIC	ω^2	L	mnl	a_{mnl}	$\lvert a_{mnl}\rvert$
			012	$-0.113 + 0.272i$	0.294
			111	$-0.478(1-i)$	0.675
1	0.385	5.065	-111	0.675	0.675
			012	$-0.261(1-i)$	0.369
			211	$0.656i$	0.656
2	1.055	3.051	-211	0.656	0.656
			211	$0.658i$	0.658
			-211	0.658	0.658
			112	$-0.237 - 0.098i$	0.256
3	1.0535	3.833	-112	$-0.098 - 0.237i$	0.256
			211	-0.505	0.505
			-211	0.505	0.505
			112	$-0.455 - 0.189i$	0.493
4	1.065	3.869	-112	$0.189 + 0.455i$	0.493

resonances in the vicinity of this crossing $L = 5, \omega^2 \approx 0.385$ (see parameters of the first BIC in table 5). According to equation (98) we have $W^{\rm L}_{012;01} = -W^{\rm R}_{012;01}$, $W^{\rm L}_{\pm 111;01} = W^{\rm R}_{\pm 111;01}\, e^{\mp i\Delta\phi}$. Therefore for the output waves interfering constructively we have to take $\Delta\phi = \pm\pi$, while fully destructive interference takes place at $\Delta\phi = 0$. This simple consideration is in excellent agreement with numerics presented in figure 24(a). Along the same line for channels 012 and ± 211 in the vicinity of $L = 3$ we have from equation (98) $W^{\rm L}_{012;01} = -W^{\rm R}_{012;01}$, $W^{\rm L}_{\pm 211;01} = W^{\rm R}_{\pm 111;01}\, e^{\mp 2i\Delta\phi}$ to open wave flux through the resonator at $\Delta\phi = \pi/2, 3\pi/2$. That conclusion fully agrees with the transmittance shown in figure 24(b). Thus, the rotation of the input waveguide strongly tunes the Fano resonance [146]. In particular, there can be a collapse of the Fano resonance when the transmission zero approaches to the transmission maximum that is the signature of the BICs (see the section 4) (figure 25).

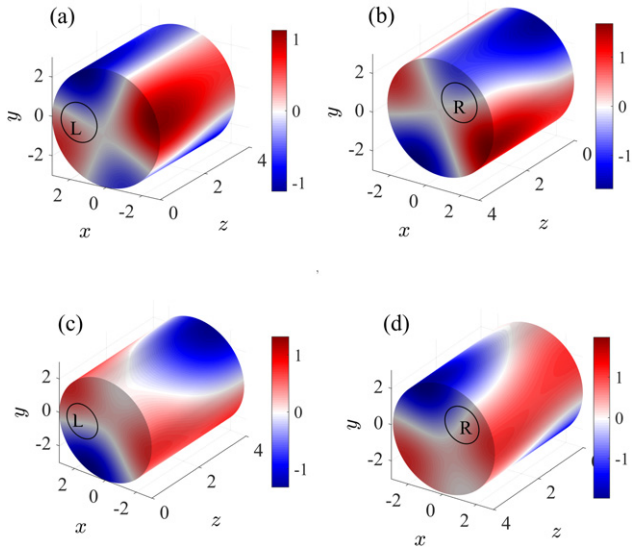

Figure 23. Patterns of BIC 3 shown from the left (a) and right (b) sides of the resonator and BIC 4 shown from the left (c) and right (d) sides of resonator on the surface of the waveguide at $\Delta\phi = \pi/4$. Reprinted from [141], Copyright (2018), with permission from Elsevier.

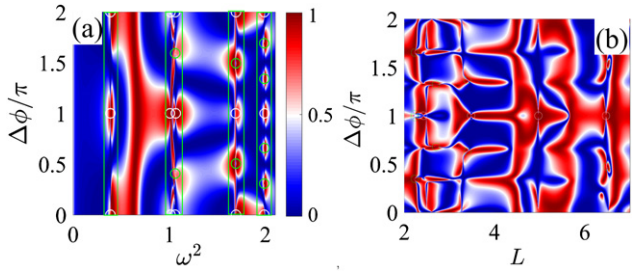

Figure 24. Transmittance of a cylindrical resonator (a) vs frequency and rotation angle $\Delta\phi$ at $L = 4$ and (b) vs length and rotation angle at $\omega^2 = 2$. The positions of the BICs are shown by open circles. Reprinted from [141], Copyright (2018), with permission from Elsevier.

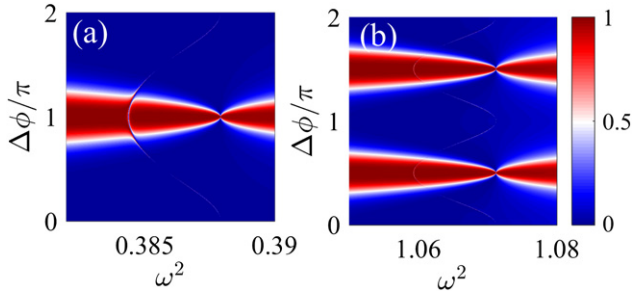

Figure 25. Transmittance vs the frequency and rotation angle in the vicinity of crossing of the modes (a) 012 and ± 111 at $L = 5$, (b) 012 and ± 211 at $L = 3$, and (c) ± 112 and ± 211, $L = 4$. Reprinted from [141], Copyright (2018), with permission from Elsevier.

Figure 26 evidences that the rotation angle $\Delta\phi = \pi/4$ is not a unique requirement for BICs to occur. In fact, we will show below analytically that there is a whole line $L = f(\Delta\phi)$ of BICs. Among them, we select four BICs shown in figure 27. Let us consider the first BIC from table 6 whose azimuthal

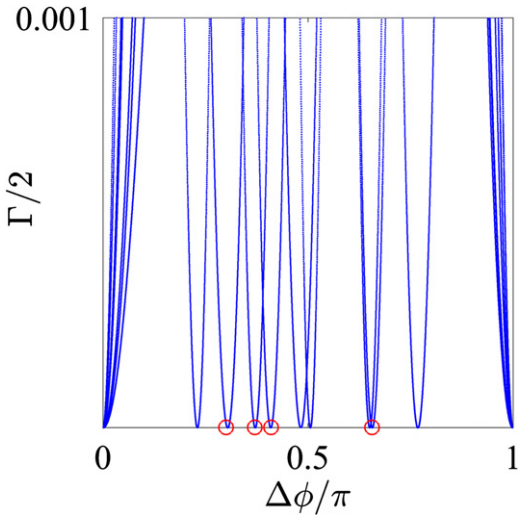

Figure 26. Evolution of resonant widths under waveguide rotation at $L = 4$. Reprinted from [141], Copyright (2018), with permission from Elsevier.

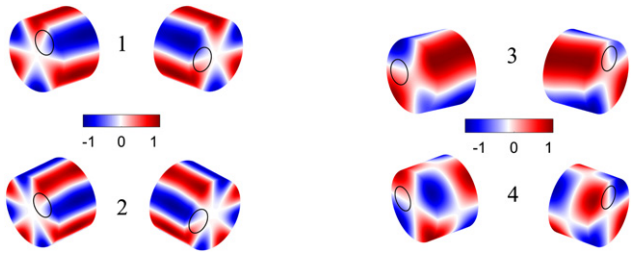

Figure 27. Patterns of BICs marked by open circles in figure 12 and listed in table 6 on the surface of the resonator at $L = 4$: 1–4. Open circles show where the left and right waveguides are attached to the resonator. Reprinted from [141], Copyright (2018), with permission from Elsevier.

dependence is given by $\cos[3(\phi - \Delta\phi/2)]$. In order to decouple this BIC from the right waveguide at $\Delta\phi = 0$ the nodal line of the BIC mode has to be positioned at $\phi = 0$, which gives us the equation $\frac{3}{2}\Delta\phi = \frac{\pi}{2}$, i.e. $\Delta\phi = \frac{\pi}{3}$. Therefore the BIC mode is $\cos[3(\phi - \pi/6)]$, which equals zero at $\phi = 0$. The left waveguide is rotated by the angle $\pi/3$ for which the BIC mode is decoupled from the left waveguide, too. Numerically according to table 6 we have $\Delta\phi = 0.308\pi$ which is close to $\pi/3$. The small difference is a contribution of the evanescent modes. Similarly, for the 2nd BIC we obtain $\cos[4(\phi - \Delta\phi/2)]$ that gives us $\Delta\phi = \pi/4$, which is close to the numerical result $\Delta\phi = 0.235\pi$ given in table 6. For the fourth BIC we obtain $\Delta\phi = \pi/2$, which also well agrees with table 6. The most interesting is the third BIC, which is superposed of two modes $\cos[2(\phi - \Delta\phi/2)]$ and $\cos[(\phi + \Delta\phi/2)]$. As a result, the BIC mode is twisted as shown in figures 23 and 27(b) and (d).

8.3. CMT theory of twisted BICs

In the vicinity of the crossings of the eigenlevels of closed cylindrical resonator framed in green in figure 21(a), it is reasonable to truncate the effective Hamiltonian (99) by only those modes which participate in the crossing, similar to the

Table 6. BICs at $L = 4$.

BIC	$\Delta\phi/\pi$	ω^2	mnl	a_{mnl}
			311	0.7056
1	0.308	1.9868	−311	$0.7056\,e^{-3i\Delta\phi}$
			411	0.705
2	0.2351	3.173 04	−411	$0.705\,e^{4i\Delta\phi}$
			211	0.6898
			−211	$-0.6898\,e^{-2i\Delta\phi}$
			121	$0.0933 + 0.1215i$
3	0.4171	1.056 88	−121	$a_{121}\,e^{i\Delta\phi}$
			211	0.7043
4	0.5055	1.688 72	−211	$0.7043\,e^{-2i\Delta\phi}$

two-level description in section 6. The only difference is that, at least, three modes participate in degeneracy in the present case. For example, let consider the case when the eigenlevel $\omega_{012}^2 = \pi^2/L^2$ crosses with the double degenerate eigenlevel $\omega_{111}^2 = \mu_{11}^2/R^2$, shown in figure 28(a) by dashed lines. The coupling matrix elements of the eigenmodes with the first propagating mode $p = 0, q = 1$ (see table 4) of the right waveguide according to equations (91), (94) and (96) equal

$$W^{\rm L}_{mnl;01} = (w_0\ w_1\ w_1), \quad w_0 = W^{\rm L}_{012;01} = \frac{1}{3}\sqrt{\frac{2}{L}}, \qquad w_1 = W^{\rm L}_{\pm111;01} = 0.269\sqrt{\frac{1}{L}} \tag{103}$$

for the given radius of the resonator. We also take into account the coupling with the first evanescent modes $p = \pm1, q = 1$ of the waveguide (see table 4):

$$W^{\rm L}_{mnl;11} = (0\ v_1\ v_2), \qquad W^{\rm L}_{mnl;-11} = (0\ v_2\ v_1),$$
$$v_1 = W^{\rm L}_{012;11} = 0.1141\sqrt{\frac{1}{L}}, \quad v_2 = W^{\rm L}_{\pm111;11} = -0.0141\sqrt{\frac{1}{L}}. \tag{104}$$

Because of the phase difference between the coupling matrix elements for left and right waveguides we immediately obtain

$$W^{\rm R}_{mnl;01} = (-w_0\ w_1\,e^{i\Delta\phi}\ w_1\,e^{-i\Delta\phi}),$$
$$W^{\rm R}_{mnl;11} = (0\ v_2\,e^{i\Delta\phi}\ v_1\,e^{-i\Delta\phi}), \tag{105}$$
$$W^{\rm R}_{mnl;-11} = (0\ v_1\,e^{i\Delta\phi}\ v_2\,e^{-i\Delta\phi}).$$

The contribution of the higher evanescent modes shown in table 4 is negligible. For the open channel $p = 0, q = 1$ the wave number $q_{01} = \omega$ while for the next closed channel $p = \pm1, q = 1$, the wave number $k_{11} = iq_{11}$, $q_{11} = \sqrt{\mu_{11}^2 - \omega^2}$ is imaginary. Then the truncated effective Hamiltonian (2) can be rewritten as follows:

$$\widehat{H}_{\rm eff} = \widehat{H}_{\rm R} + q_{11}\sum_{C={\rm L,R}}\sum_{p=\pm1}\widehat{W}^C_{p=\pm1,1}\{\widehat{W}^C_{p=\pm1,1}\}^\dagger - i\omega \times \sum_{C={\rm L,R}}\widehat{W}^C_{01}\{\widehat{W}^C_{01}\}^\dagger = \widehat{\widetilde{H}}_{\rm R} - i\omega\widehat{\Gamma}, \tag{106}$$

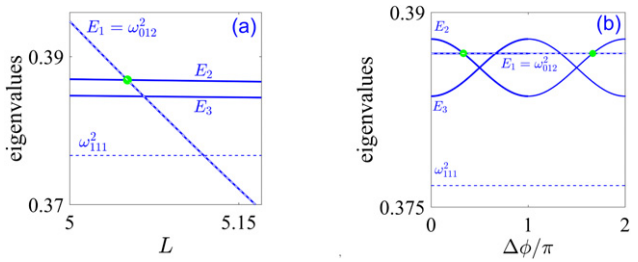

Figure 28. The eigenvalues ω_{012}^2 and ω_{111}^2 of the closed resonator are shown by dashed lines while the eigenlevels (109) shifted by the evanescent modes are shown by solid lines. (a) The eigenvalues (109) vs the resonator length at $\phi = \pi/3$ and (b) vs rotation angle at $L = 5.0512$. Reprinted from [141], Copyright (2018), with permission from Elsevier.

where the Hermitian term

$$\widehat{\widetilde{H}}_{\rm R} = \begin{pmatrix} \omega_{012}^2 & 0 & 0 \\ 0 & \omega_{111}^2 + 2q_{11}(v_1^2 + v_2^2) & 2q_{11}v_1v_2(1 + e^{-2i\Delta\phi}) \\ 0 & 2q_{11}v_1v_2(1 + e^{2i\Delta\phi}) & \omega_{111}^2 + 2q_{11}(v_1^2 + v_2^2) \end{pmatrix} \tag{107}$$

is the Hamiltonian of the resonator coupled to the evanescent modes. The anti-Hermitian part takes the following form:

$$\widehat{\Gamma} = \begin{pmatrix} 2w_0^2 & w_0w_1(1 - e^{i\Delta\phi}) & w_0w_1(1 - e^{-i\Delta\phi}) \\ w_0w_1(1 - e^{-i\Delta\phi}) & 2w_1^2 & w_1^2(1 + e^{-2i\Delta\phi}) \\ w_0w_1(1 - e^{i\Delta\phi}) & w_1^2(1 + e^{2i\Delta\phi}) & 2w_1^2 \end{pmatrix}. \tag{108}$$

The eigenvalues of the Hermitian part of the Hamiltonian (107) can be easily found as

$$E_1 = \omega_{012}^2, \quad E_{2,3} = \omega_{111}^2 + 2q_{11}[v_1^2 + v_2^2 \pm 2v_1v_2\ \cos\ \Delta\phi]. \tag{109}$$

Thus the evanescent modes of the waveguides non-coaxially attached to the cylindrical resonator lift the degeneracy of eigenmodes ±111 as shown in figure 28 by solid lines. The degeneracy is restored for $\Delta\phi = \pi/2, 3\pi/2$. The corresponding eigenmodes of the Hamiltonian (107) are the following:

$$\mathbf{X}_1 = \begin{pmatrix} 1 \\ 0 \\ 0 \end{pmatrix}, \quad \mathbf{X}_2 = \frac{1}{\sqrt{2}}\begin{pmatrix} 0 \\ -e^{-i\Delta\phi} \\ 1 \end{pmatrix}, \quad \mathbf{X}_3 = \frac{1}{\sqrt{2}}\begin{pmatrix} 0 \\ e^{-i\Delta\phi} \\ 1 \end{pmatrix}. \tag{110}$$

Next, let us consider the BIC in the truncated version (106). The point of the BIC can be easily diagnosed by a zero resonant width as shown in figure 29. For $\Delta\phi = \pi/4$, the BIC occurs at $L = L_c = 5.0512$ marked by closed green circle in figure 29(a). Respectively at $L = L_c$, the BIC occurs at $\Delta\phi = \pi/4$ and $\Delta\phi = 2\pi - \pi/4$. These points are seen in the insert in figure 29(b).

For $\Delta\phi = 0$ both the continua of the left and right waveguides coincide to result in the SP BIC superposed of degenerate eigenmodes of the closed resonator ψ_{111} and ψ_{-111} to be in the following form:

$$\psi_{\rm BSC}(r, \phi, z) = AJ_1(\mu_{11}r)\sin(\pi z/L)\sin\ \phi, \tag{111}$$

which always has zero coupling with the propagation mode $\psi_{01}(\rho, \alpha, z)$ shown in table 4. As seen from equation (111) this conclusion also holds true for $\Delta\phi = \pi$. These BICs are trivial SP ones for arbitrary resonator length.

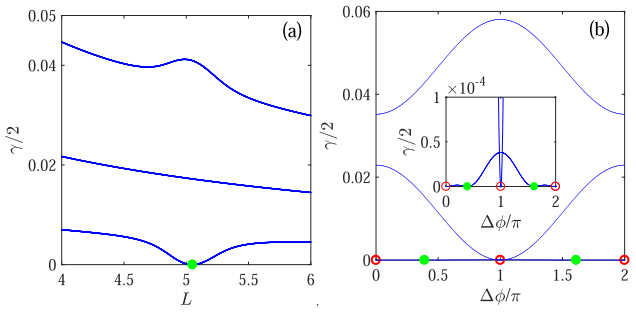

Figure 29. The resonant width vs (a) the resonator length at $\Delta\phi = \pi/4$ and (b) rotation angle at $L = 5.0512$. Open circles show the SP BICs, closed circles the FW BICs. Reprinted from [141], Copyright (2018), with permission from Elsevier.

As soon as $\Delta\phi \neq 0$ the continua become different to destroy the SP BICs. It could be expected that in the case of two waveguides, the point of threefold degeneracy where the ω_{012} crosses the double degenerate ω_{111} as shown in figure 28(a) is a BIC point in accordance with the above consideration. However the BIC point where the resonant width turns to zero (see figure 29) does not coincide with this point. The computation on the basis of a full basis effective Hamiltonian gives the same result. In fact, the evanescent modes split the eigenvalues (109). Respectively the point of threefold degeneracy $\omega^2_{111} = \omega^2_{012}(L)$ splits into two double degenerate points $E_1(L) = E_2(L, \Delta\phi)$ and $E_1(L) = E_3(L, \Delta\phi)$. As shown in figure 28(a) the first case exactly corresponds to the BIC point but not the second case.

In the first case we can superpose the eigenmodes (110) as $a\mathbf{X}_1 + b\mathbf{X}_2$ and require zero coupling of this superposed mode with the left waveguide

$$aw_0 + \frac{b}{\sqrt{2}} w_1 (1 - \mathrm{e}^{-\mathrm{i}\Delta\phi}) = 0 \qquad (112)$$

according to equations (103) and (110). It is easy to show that the coupling with the phase-shifted continuum of the left waveguide takes the *same* form as equation (112). Thus, the BIC has the following form:

$$\psi_{\mathrm{BSC}} = w_1(1 - \mathrm{e}^{-\mathrm{i}\Delta\phi})\psi_{012} + w_0(\mathrm{e}^{-\mathrm{i}\Delta\phi}\psi_{111} - \psi_{-111}). \qquad (113)$$

Substituting eigenmodes (94) into equation (113) we obtain

$$\psi_{\mathrm{BSC}} = 2\mathrm{i}\,\mathrm{e}^{-\mathrm{i}\Delta\phi/2}\left[w_1\ \sin(\Delta\phi/2)\psi_{01}(r)\psi_2(z) + w_0\ \sin(\phi - \Delta\phi/2)\psi_{11}(r)\psi_1(z)\right]. \qquad (114)$$

The BIC point is given by the equation $E_1(L) = E_2(L, \Delta\phi)$ which gives rise to a line of the BSC in the parametric space L and $\Delta\phi$ shown in figure 30.

Thus, we have shown the occurrence of the BICs embedded into two continua which differ by their phase in the point of a twofold degeneracy. It is important to stress that this degeneracy refers to the eigenlevels of the Hamiltonian (107) of the cylindrical resonator modified by the evanescent modes of the attached waveguides. This is a necessary condition for existence of BIC, but not sufficient. Indeed let us consider the another point of degeneracy, $E_1 = E_3$ (see figure 28(a)). At this point we adjust the superposition $a\mathbf{X}_1 + b\mathbf{X}_3$ for cancellation of the coupling with both continua. The analogue of equation (112) takes the following form:

$$\pm aw_0 + \frac{b}{\sqrt{2}} w_1 (1 + \mathrm{e}^{\mathrm{i}\Delta\phi}) w_1 = 0. \qquad (115)$$

These equations cannot be fulfilled simultaneously to forbid this degeneracy point as the BIC point. By the use of equation (100) and truncated effective Hamiltonian (106) we calculated the transmittance with the results presented in figure 31. Comparison to figures 21(b) and (c) shows that all features of the transmittance can be well reproduced in the vicinity of the BICs by the use of a truncated basis.

One can also see from figures 31 and 32 that the resonant features follow the real parts of the complex eigenvalues of

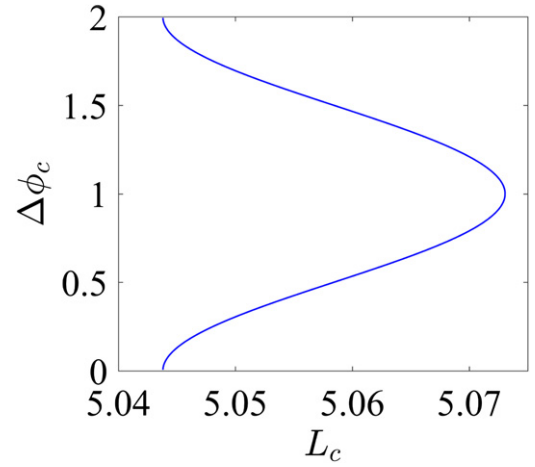

Figure 30. Line of the BICs in the parametric space of the resonator length and rotation angle $\Delta\phi$. Reprinted from [141], Copyright (2018), with permission from Elsevier.

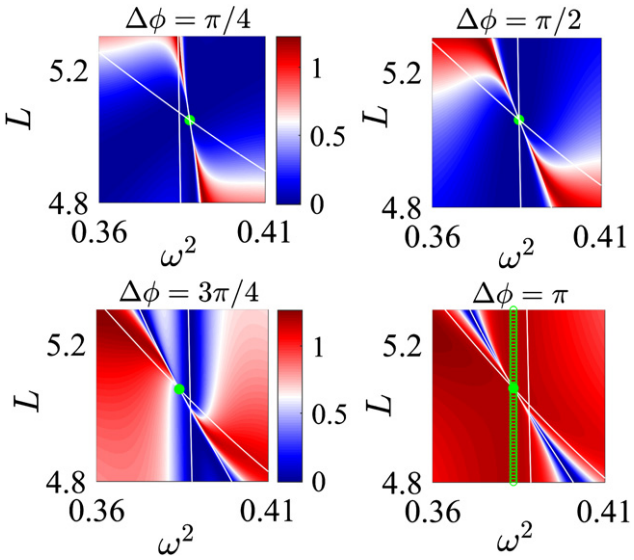

Figure 31. (a) Transmittance vs frequency and resonator length at four fixed rotation angles. Solid green lines show the resonances defined by real part of the complex eigenvalues of the effective Hamiltonian (106). Closed circles mark the BSCs which exactly correspond to points of degeneracy of the eigenlevels (109). Reprinted from [141], Copyright (2018), with permission from Elsevier.

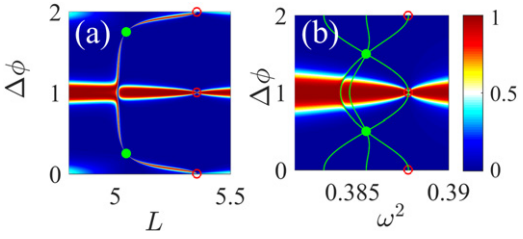

Figure 32. (a) Transmittance vs the resonator length and rotation angle for the frequency tuned to the frequency ofBIC $\omega_c^2 = 0.388$. (b) Transmittance vs the frequency and rotation angle for the length tuned to the BIC length $L_c = 5.048$. Closed green circles mark BIC 1 resulted by crossing of eigenlevels (109) ω_{012}^2 and ω_{pm112}^2, open red circles mark the SP BICs (111). Reprinted from [141], Copyright (2018), with permission from Elsevier.

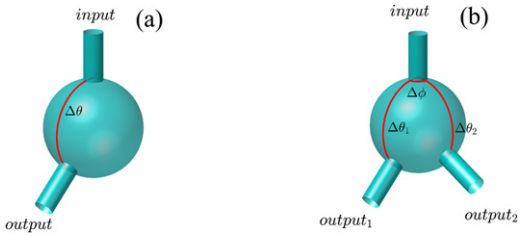

Figure 33. Spherical cavity of radius R with (a) two and (b) three attached cylindrical waveguides of the same radii r.

the effective non-Hermitian Hamiltonian (106) when $\Delta\phi \neq 0$. Figure 32 shows the fine features of the transmittance vs two parameters for the third parameter exactly tuned to the BIC. Figure 32(a) demonstrates a Fano resonance collapse in the parametric space of length and rotation angle at the BIC point $L_c = 5.048$ and $\Delta\phi_c = \pi/4$, with the frequency exactly tuned to the BIC $\omega_c = 0.3873$. Figure 32(b) shows the transmittance vs the frequency and the rotation angle for the length of the resonator tuned to the BIC length $L_c = 5.0584$. Figures 32(a) and (b) show that the resonator is blocked when $\Delta\phi = 0$ and open when $\Delta\phi = \pi$. We skip here the case when the mode ± 112 crosses the mode ± 211 and refer the reader to the chapter in the book by [147]. Despite the truncated effective Hamiltonian including four states, this case still allows for the analytical treatment of BICs.

9. Spherical cavity

In this section we consider the FW BICs which exist only due to the contribution of the evanescent modes of waveguides. Such an example is an open spherical cavity, as shown in figure 33, which presents a system consisting of two subsystems with incompatible symmetries. The continua obey cylindrical symmetry while the resonator follows spherical symmetry. The integrable spherical cavity has the only scale to vary the sphere radius R, which only scales the eigenvalues by the factor $\frac{1}{R^2}$. The eigenmodes are spherical functions which are $2l+1$-fold degenerated, where l is the orbital index. Let us attach two cylindrical waveguides, as shown in figure 33(a), that fully remove this degeneracy. Therefore, it seems that the FW mechanism for the BICs cannot be applied here due to an avoided crossing. The continua of the waveguides in the form of propagating Bessel modes transform the discrete eigenfrequencies of the closed cavity into the complex resonant frequencies whose positions depend on the overlapping of the spherical functions with the Bessel modes. In turn, if the waveguides are angled by $\theta \neq \pi$, the variation over that angle can give rise to avoided crossings of resonant modes with different l, resulting in the FW BICs.

In order to demonstrate this effect, we use the CMT with the Neumann boundary conditions applicable for the transmission of acoustic or EM waves with TM polarization [112]. It is easy to find a solution of the Helmholtz equation in spherical coordinates, so the eigenfunctions of a spherical cavity are the following:

$$\Psi_{lmn} = \Psi_{ln}(r) Y_{lm}(\theta, \phi), \tag{116}$$

$$\Psi_n(r) = \frac{1}{R_s^{3/2}} \sqrt{\frac{2}{\kappa_{l+1/2,n}^2 - n(n+1)}} \times \frac{\kappa_{l+1/2,n}}{J_{l+1/2}(\kappa_{l+1/2,n})} J_{l+1/2}\left(\frac{\kappa_{l+1/2,n} r}{R}\right), \tag{117}$$

$$Y_{lm}(\theta, \phi) = \sqrt{\frac{(2l+1)(l-m)!}{4\pi(l+m)!}} P_{lm}(\cos\,\theta) \exp(m\phi), \tag{118}$$

where r, θ, ϕ are the spherical coordinates, R is the spherical cavity radius, Y_{lm} are the spherical harmonics, $P_{lm}(\cos\theta)$ are the associated Legendre polynomials, $J_{l+1/2}$ are the Bessel functions, and $\kappa_{l+1/2,n}$ are the roots of the equation $\frac{\mathrm{d}J_{l+1/2,n}(\frac{\kappa_{l+1/2}\, n^r}{R_s})}{\mathrm{d}r}\Big|_{r=R_s}$. Respective eigenfrequencies of the closed spherical resonator are given as

$$\omega_{nl}^2 = \kappa_{l+1/2,n}^2 / R^2, \tag{119}$$

which are $2l+1$-fold degenerates over the azimuthal index $-l < m < l$. All the quantities are dimensionless and expressed in terms of the cylindrical waveguides radius a. The dimensionless frequency ω is expressed through the dimensional one $\tilde{\omega}$ as follows: $\omega = \tilde{\omega} a/s$ in acoustics or $\omega = cka$, where s/c is the sound/light velocity.

The eigenfunctions of the cylindrical waveguides are

$$\psi_{pq}^{(C)}(\rho, \alpha, z) = \psi_{pq}^{(C)}(\rho) \frac{1}{\sqrt{2\pi k_{pq}^{(C)}}} \exp(\mathrm{i}p\alpha + ik_{pq}^{(C)} z),$$

$$\psi_{pq}^{(C)}(\rho) = \begin{cases} \dfrac{\sqrt{2}}{aJ_0(\mu_{0q})} J_0\left(\dfrac{\mu_{0q}\rho}{a}\right), & p = 0, \\ \sqrt{\dfrac{2}{\mu_{pq}^2 - p^2}} \dfrac{\mu_{pq}}{aJ_p(\mu_{pq})} J_p\left(\dfrac{\mu_{pq}\rho}{a}\right), & p = 1, 2, 3, \ldots, \end{cases} \tag{120}$$

where ρ, α are the polar coordinates in the $x0y$-plane in the waveguides reference system, $J_p(x)$ are the cylindrical Bessel functions of the first kind, μ_{pq} is the qth root of equation $\frac{\mathrm{d}J_p(\mu_{pq}\rho)}{\mathrm{d}\rho}\Big|_{\rho=a} = 0$ imposed by the Neumann boundary condition on the walls of sound hard cylindrical waveguide, C enumerates input and output waveguides, and $k_{pq}^{(C)}$ is the wave number:

$$k_{pq}^{(C)} = \sqrt{\omega^2 - \mu_{pq}^2/a^2}. \tag{121}$$

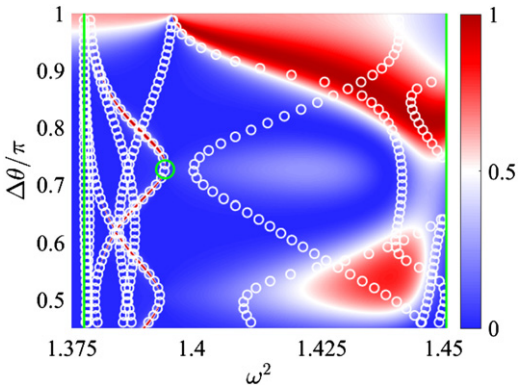

Figure 34. Transmittance of the spherical resonator vs the frequency of the injected wave and displacement angle of the second waveguide. Small open white circles show the real part of eigenfrequencies of open cavity vs the second waveguide displacement angle. The large open green circle indicates the BIC point with the collapse of the Fano resonance.

In order to write the non-Hermitian effective Hamiltonian, it is necessary to calculate the coupling coefficients between the modes propagating in the waveguides and the eigenmodes of the spherical cavity. For the waveguide connected to the pole of the resonator, the coupling matrix elements can be calculated as follows [112, 141]:

$$W_{lmn,pq} = \Psi_{ln}(r=R)\int_0^{2\pi} \mathrm{d}\phi \times \int_0^1 \rho\,\mathrm{d}\rho\psi_{pq}(\rho,\phi)Y_{lm}(\theta(\rho,\phi),\phi), \quad (122)$$

where ρ is the radius in the cylindrical reference frame, $\phi=\alpha$ is the azimuthal angle, and θ is the polar angle in the spherical reference frame. To perform this integration, one has to express the spherical coordinates in terms of the cylindrical ones, which can be done by a simple mathematical transformation. We assume here that the integration is carried out over the circular interface between the waveguides and that the cavity in the limit $R \gg 1$. Then the integration interface can be approximated by a flat circle.

The calculation of the coupling matrix elements for asymmetrically connected waveguides is somewhat difficult. We assume that these waveguides are also connected to the pole of the spherical resonator and then rotate the cavity eigenfunctions, which are physically equivalent to rotation of the waveguides. For that procedure we use the Wigner D-matrix:

$$D^l_{mk}(\alpha,\beta,\gamma) = \exp(-\mathrm{i}k\alpha)d^l_{mk}(\beta)\exp(-\mathrm{i}m\gamma), \quad (123)$$

where α,β,γ are the Euler's angles and $d^l_{mk}(\beta)$ is the small Wigner matrix:

$$d^l_{mk} = \sqrt{\frac{(l-m)!(l+m)!}{(l-k)!(l+k)!}}\sum_{s=\max(0,k-m)}^{\min(l-m,l+k)}(-1)^{m-k+s}, \quad (124)$$

$$\binom{l+k}{s}\binom{l-k}{m-k+s}\cos^{2l-m+k-2s}\times\left(\frac{\beta}{2}\right)\sin^{m-k+2s}\left(\frac{\beta}{2}\right). \quad (125)$$

Then the rotated spherical harmonic can be expressed through the non-rotated one as follows:

$$\tilde{Y}^l_m(\theta,\phi) = \exp(-\mathrm{i}m\gamma)\sum_{k=-l}^{l}\exp(-\mathrm{i}k\alpha)d^l_{mk}(\beta)Y^l_k(\theta',\alpha'), \quad (126)$$

and the coupling matrix elements of the asymmetrically connected waveguides are the following:

$$\tilde{W}_{lmn,pq} = \exp(-\mathrm{i}m\gamma)\sum_{k=-l}^{l}\exp(-\mathrm{i}k\alpha)d^l_{mk}W_{lkn,pq}. \quad (127)$$

Next, we write the effective non-Hermitian Hamiltonian of the system, which is the result of projection of the entire Hilbert space of the system 'waveguides + cavity' onto the spherical cavity subspace

$$H_{\mathrm{eff}} = H_B - \mathrm{i}\sum_C\sum_{pq}k^{(C)}_{pq}W^{(C)}_{pq}W^{(C)\dagger}_{pq}, \quad (128)$$

where the last term is given by the coupling matrix elements (122). Then the transmission coefficients from the channel pq of the waveguide (C) to the channel $p'q'$ of the waveguide (C') are given by the following equation [112, 141]:

$$t^{(CC')}_{pq;p'q'} = 2\mathrm{i}\sqrt{k^{(C)}_{pq}k^{(C')}_{p'q'}}\sum_{lmn}\sum_{l'm'n'}W^{(C)}_{lmn;pq} \times \frac{1}{\omega^2 - H_{\mathrm{eff}}}W^{(C')*}_{l'm'n';p'q'}. \quad (129)$$

9.1. Two waveguides

An attachment of waveguides lifts the $2l+1$-fold degeneracy of the eigenvalues of the closed spherical cavity as demonstrated in figure 34, where the real parts of the effective Hamiltonian (128) complex eigenvalues are plotted by small open circles versus the rotation angle $\Delta\theta$. One can see from figure 34 that the rotation of the second waveguide relative to the first waveguide splits the resonances. It is more important, however, that such a rotation gives rise to the avoided crossing of resonances with different orbital indices l and respectively to the FW BIC, which is marked by large open circle. Figure 34 also shows the transmittance versus the injected wave frequency and the second waveguide displacement angle $\Delta\theta$. One can see that the narrow resonant peaks follow the resonant frequencies marked by open circles. The small resonant widths are the result of normalization coefficients of the eigenmodes of the spherical cavity (120) proportional to $\frac{1}{R^{3/2}}$. As a result, the coupling matrix elements (122) have the same factor and the resonant widths which are given by squared coupling matrix elements turn out to be proportional to $\frac{1}{R^3}$, while the distance between the eigenfrequencies of H_B are proportional to $\frac{1}{R^2}$. Therefore for $R \ll 1$, we have the case of weak coupling of the sphere with the waveguide continuum.

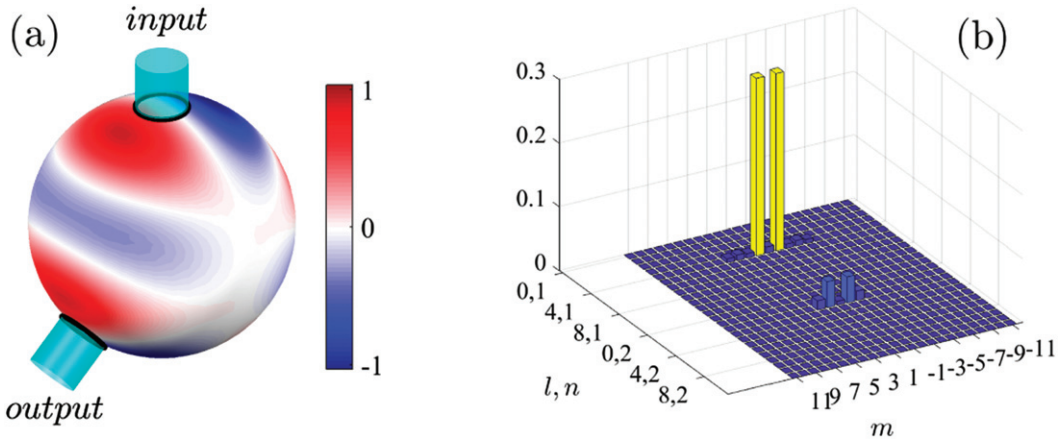

Figure 35. (a) The pressure field of the FW BIC at $\omega = 1.3937$ and $\Delta\theta = 0.727\pi$. (b) The modal decomposition of the BIC.

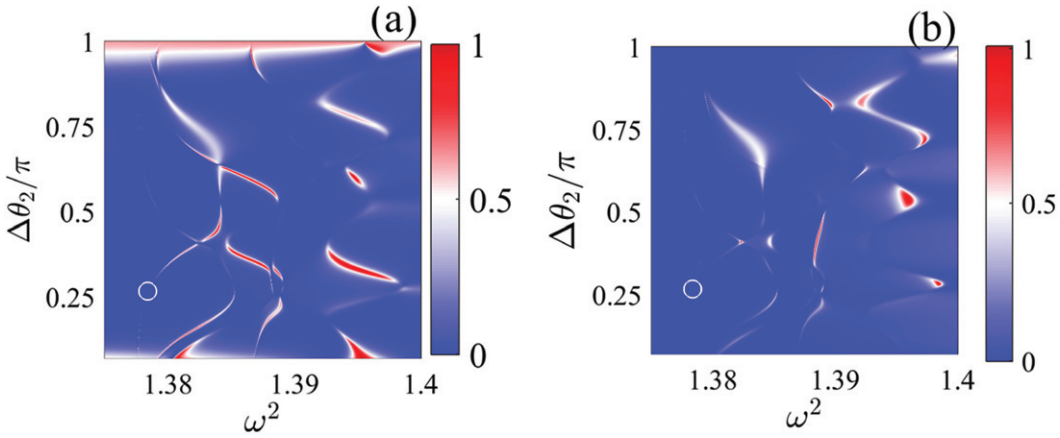

Figure 36. Transmittance between 'input' and 'output 1' (a) and 'input' and 'output 2' vs frequency and the displacement angle $\Delta\theta_2$ of the third waveguide for $\Delta\theta_1 = \pi/4$. The displacement angle of the second waveguide is $\Delta\theta_1 = 3\pi/4$. Circles mark the FW BICs.

The collapse of the Fano resonance, i.e. the coincidence of the unit and zero transmittance, is the signature of the BIC [17, 34]. Figure 34 shows one of these events at which the imaginary part of the complex eigenvalues of the non-Hermitian effective Hamiltonian vanishes. A major part of the BICs in the case of two waveguides are SP. These SP BICs can be obtained by simple rotation of the eigenfunctions of the closed spherical resonator in order to achieve the orthogonality of the eigenfunction to the mode of waveguide. We do not show here the SP BICs which coincide with the rotated eigenmode of the closed cavity by use of the Wigner *D*-matrix.

However, figure 34 marks the FW BIC at point $\Delta\theta = 0.7\pi$, $\omega = 1.378$ by an open green circle. Figure 35(a) shows the FW BIC wave function (the pressure field/magnetic field) on the resonator surface. One can see from the nodal lines on the surface of the sphere that the BIC mode is decoupled from the first continuum of the waveguide with indices $p = 0, q = 1$. The modal expansion of this FW BIC over the eigenmodes of the closed spherical cavity $\Psi_n l(r) Y_{lm}(\theta, \phi)$ is shown in figure 35(b). The eigenmodes with quantum numbers $l = 4, m = \pm 1, n = 1$ and $l = 1, m = \pm 1, n = 2$ contribute to the FW BIC. Thus, the FW BIC is the result of the fully destructive interference of resonant modes with different orbital indices, despite that the eigenmodes of the closed spherical cavity with different orbital momentums l have different frequencies (121).

9.2. Three waveguides

Although the position of the second waveguide relative to the first one at the pole of the sphere is given by two angles in general, only the polar angle $\Delta\theta_1$ is physically relevant for resonances and, in particular, for the BICs. The introduction of the third waveguide as shown in figure 33(b) substantially changes the effects of the continua on the resonances because of three relevant angles, two polar angles $\Delta\theta_1$ and $\Delta\theta_2$ and one azimuthal angle $\Delta\phi$. Figures 36 and 37 show the transmittance versus the frequency of the injected wave and rotation angles $\Delta\theta_2$ and $\Delta\phi$ of the third waveguide, which evident the importance of the mutual orientations of all three waveguides. The regions in which avoiding of the crossing phenomenon occurs, as well as the collapse of the Fano resonance, are highlighted by the frames in figure 37. One can see that these phenomena take place irrespective of which waveguide goes wave.

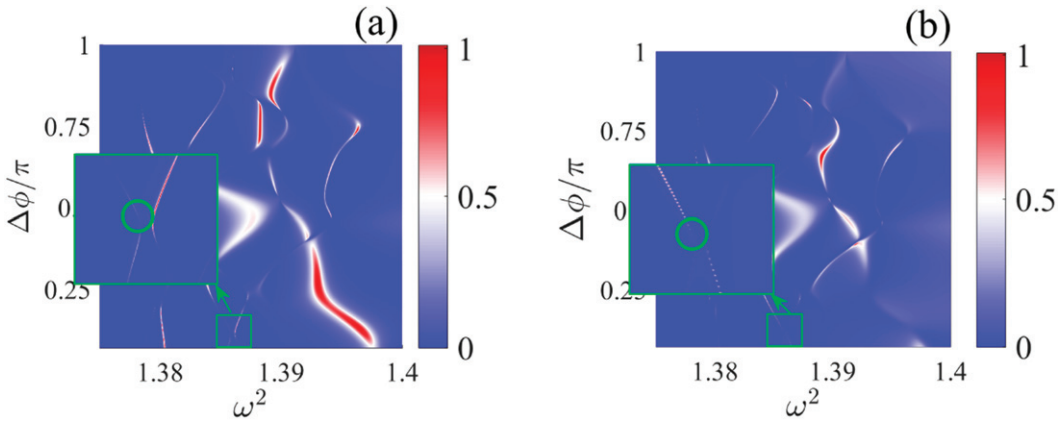

Figure 37. Transmittance between 'input' and 'output 1' (a) and 'input' and 'output 2' vs frequency and the displacement angle $\Delta\theta_2$ of the third waveguide for $\Delta\theta_1 = \sqrt{5}$.

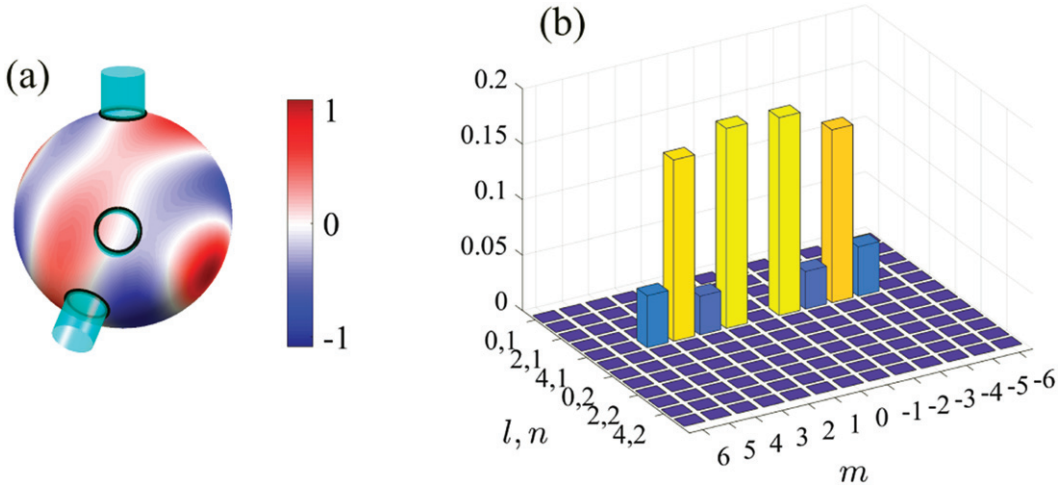

Figure 38. (a) The BIC pattern (pressure field) on the surface of the spherical cavity at the BIC point with $\omega = 1.385\,75$, $\Delta\theta_1 = \sqrt{5}$, $\Delta\theta_2 = \sqrt{2}$ and $\Delta\phi = 0.1222\pi$. (b) The modal decomposition of the BIC.

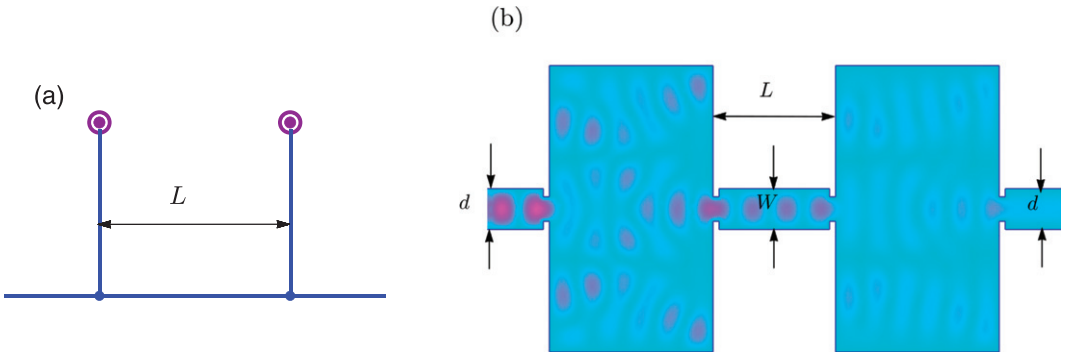

Figure 39. (a) 1D wire with two off-channel cavities. (b) 2D wire with two inserted identical resonators.

The circles in figures 36 and 37 mark the position of the FW BIC whose pattern in the form of surface pressure/a magnetic field on surface of the resonator is shown in figure 38(a). The amplitudes a_{nlm} of the superposition of the spherical harmonics are chosen in so way that the nodal lines shown in white pass through the overlapping areas of waveguides with the spherical cavity. As a result, the coupling constants of the FW BIC with the first propagating channel or continuum vanish.

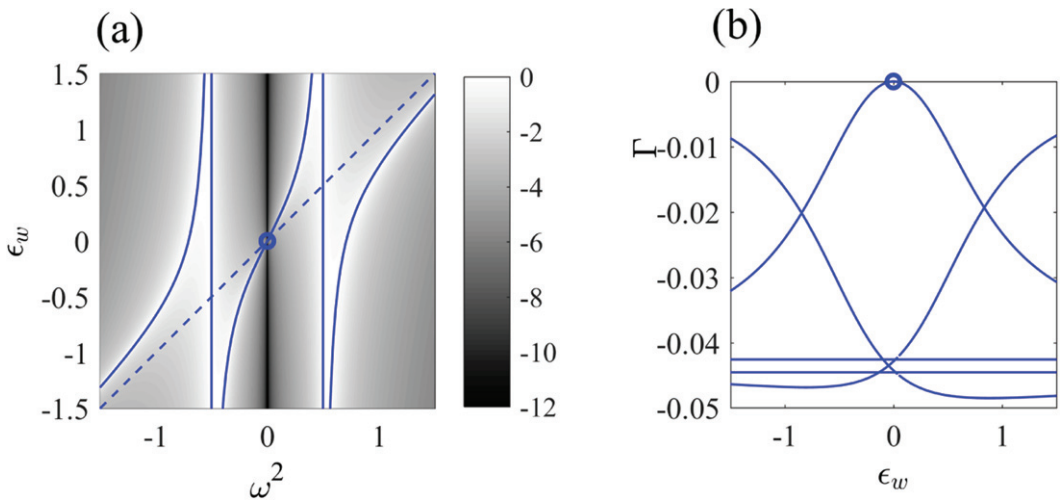

Figure 40. (a) The transmittance in log scale through the double resonator vs the frequency ϵ_w of wire and incident frequency $E = \omega^2$. (b) The resonant widths as dependent on ϵ_w at $E = 0.5$ at the following parameters of the system: $\epsilon_{1,2} = \pm 1/2, v = 0.5, u = 1/4$.

10. The Fabry–Perot mechanism of BICs in the system of two coupled resonators

If the double-barrier resonant structure had infinitely high barriers, the eigenmodes were localized between the barriers. For a finite height of barriers, these eigenmodes transform into the resonant modes with finite resonant widths defined by the probability of tunneling. Such a one-dimensional QM structure has one-to-one equivalency with the Fabry–Perot resonator (FPR) [148] and has no BICs as was discussed in section 4. Let us substitute the two-dimensional resonators instead of the barriers or mirrors in the FPR as presented in figure 39.

We start with the simplest case of a 1D wire to which two off-side or off-channel cavities are attached, as illustrated in figure 39(a). The case of a single off-channel defect realizes the simplest way for Fano resonance due to interference of two wave paths, a direct path over the wire and a second path through the off-channel defect. As a result, this gives rise to N transmission zeros at $\omega = \omega_n, n = 1, 2, \ldots, N$, where N is the number of eigenfrequencies of the defect [111, 149]. Thus, the off-channel defects can serve as ideal Fano mirrors and support BICs provided that an integer of half-waves is placed between mirrors, i.e.

$$\pi cn = \omega_n L, \tag{130}$$

where c is the light velocity. Therefore, the underlying mechanism of the bound states in the one-dimensional wire with two off-channel defects are (i) transmission zeroes of each defect at definite frequency, or perfect reflections, i.e. mirrors, and (ii) the integer number of the half waves between the mirrors. This mechanism, exclusively transparent, for the bound states which we call as the FP BIC, was applied to a photonic crystal structure with a waveguide coupled with two cavities [40, 47, 150, 151]. The same mechanism of BICs was exploited in photonic crystal systems in which one-dimensional arrows of dielectric rods [40, 46, 48] and two-dimensional periodical PhC structures in the form of perforated slabs or dielectric particles [49, 66] served as perfectly reflecting mirrors.

A different way is to implement two-dimensional cavities into waveguide as shown in figure 39(b) [43–45]. Each resonator has transmission zeroes [152] at some frequencies to serve as FP mirrors. Therefore the total system consists of two cavities and a wire between them. In the simplest form, the Hamiltonian of a closed system has the following matrix structure:

$$H_B = \begin{pmatrix} \epsilon_1 & 0 & u & 0 & 0 \\ 0 & \epsilon_2 & u & 0 & 0 \\ u & u & \epsilon_w & u & u \\ 0 & 0 & u & \epsilon_2 & 0 \\ 0 & 0 & u & 0 & \epsilon_1 \end{pmatrix}. \tag{131}$$

We can consider the eigenlevel of the wire ϵ_w to be the parameter by which the system can be controlled.

The minimal rank of matrix (131) is five, so that we can let E_n and $|n\rangle$ with $n = 1, \ldots, 5$ denote the five eigenlevels and eigenstates of (131). The amplitudes $\langle j = 1, 2|n\rangle$ describe the left resonator, $\langle j = 3|n\rangle$ the waveguide, and $\langle j = 4, 5|n\rangle$ the right resonator. Two semi-infinite waveguides attached to the resonators provide continua and therefore transform the states of the closed system into resonances which are described by the effective non-Hermitian Hamiltonian [111]:

$$\langle m|H_{\text{eff}}|n\rangle = E_m\delta_{mn} - 2\pi\mathrm{i}(V_{\text{L}}(m)V_{\text{L}}(n) + V_{\text{R}}(m)V_{\text{R}}(n)) \tag{132}$$

with the coupling matrix elements

$$\begin{aligned} V_{\text{L}}(m) &= v(k)\sum_{j=1,2}\langle j|m\rangle, \\ V_{\text{R}}(m) &= v(k)\sum_{j=4,5}\langle j|m\rangle, \end{aligned} \tag{133}$$

where the factors $\sqrt{\frac{k}{2\pi}}$ originated from the normalization of propagating states of 1D waveguides are absorbed by $v(k)$.

The transmittance through the system given by equation (129) is shown in figure 40(a) at the log scale in order to follow transmission zeros and resonances. Because

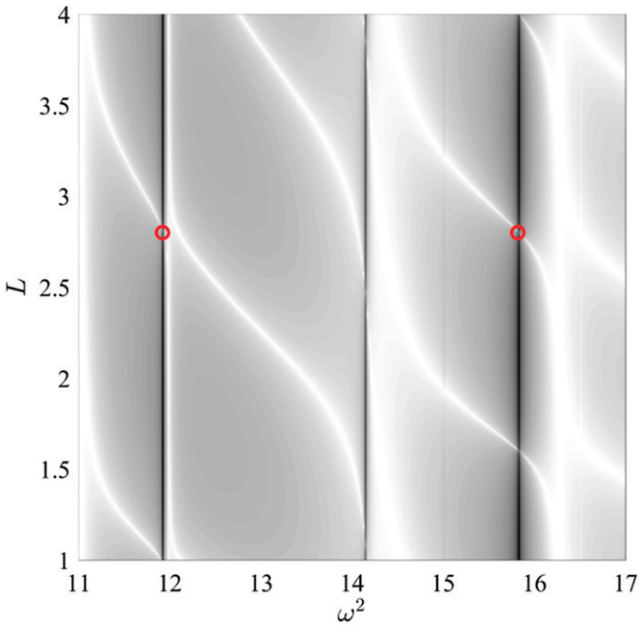

Figure 41. The transmittance in log scale of the double resonator shown in figure 39(b) versus the frequency and length of the waveguide between the resonators. The bold red open circles mark the two points of the BICs shown in figure 42.

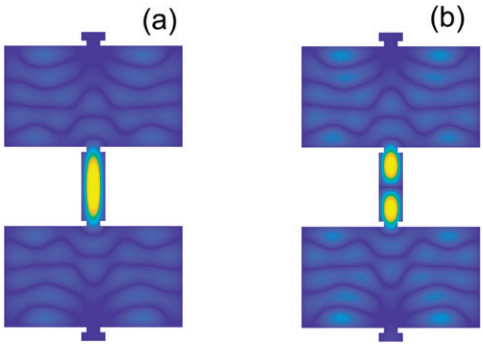

Figure 42. BICs at the points marked by the red open circles in figure 41: (a) at $\omega^2 = 11.92$ and $L = 2.8$ and (b) $\omega^2 = 15.83$ and $L = 2.83$.

of the small coupling constant $v(k) = 0.5\sqrt{\frac{k}{2\pi}}$, the transmittance demonstrates resonant behavior which follows the eigenlevels of the Hamiltonian (131) of the closed system:

$$E_{1,5} = \pm\eta, \qquad E_2 = \epsilon_1, \qquad E_3 = 0, \qquad E_4 = \epsilon_2. \tag{134}$$

The eigenvalues 2 and 4 of the effective Hamiltonian are independent of the wire's eigenvalue ε_w, while those of the other states depend on it. The eigenvalue 3, lying in the middle of the spectrum, crosses the transmission zero at

$$\epsilon_w = \epsilon_b = \frac{\epsilon_1 + \epsilon_2}{2} = 0. \tag{135}$$

At this eigenvalue we observe the collapse of the Fano resonance that witnesses the BIC fully agreeing with the turning to zero of the resonant width as seen from figure 40(b).

However, the question still remains as to where the BIC is localized: in the wire between the resonators or entirely in whole structure including resonators. It might seem that the latter is correct taking into account that the resonator provides large room for localization. Below, by use of exact analytic equations, we show that the first answer is correct, at least in the present model case of 1D wire. The eigenstates of the Hamiltonian (131) are the following:

$$\begin{aligned}
\langle 1| &= \frac{\sqrt{2}u}{\eta}\left(\frac{u}{\eta-\Delta\epsilon},\ \frac{u}{\eta+\Delta\epsilon},\ -1,\ \frac{u}{\eta+\Delta\epsilon},\ \frac{u}{\eta-\Delta\epsilon}\right)\\
\langle 2| &= \frac{1}{\sqrt{2}}(1,\ 0,\ 0,\ 0,\ -1)\\
\langle 3| &= \frac{u}{\eta}\left(1,\ -1,\ \frac{\Delta\epsilon}{u},\ -1,\ 1\right)\\
\langle 4| &= \frac{1}{\sqrt{2}}(0,\ 1,\ 0,\ -1,\ 0)\\
\langle 5| &= \frac{\sqrt{2}u}{\eta}\left(\frac{u}{\eta+\Delta\epsilon},\ \frac{u}{\eta-\Delta\epsilon},\ 1,\ \frac{u}{\eta-\Delta\epsilon},\ \frac{u}{\eta+\Delta\epsilon}\right)
\end{aligned}, \tag{136}$$

where $\eta^2 = \Delta\epsilon^2 + 4u^2, \Delta\varepsilon = (\epsilon_2 - \epsilon_1)/2$. Substituting (136) into (133) we obtain

$$\langle m|V|E, C = \mathrm{L,R}\rangle = v\sqrt{\frac{k}{8\pi}}\left(1\ \pm 1\ \frac{\Delta\epsilon}{u}\ \pm 1\ 1\right) \tag{137}$$

for the elements of the coupling matrix. One can see that under the conditions (135), the wire decouples from the rest of the system with zero imaginary parts of the third eigenvalue of H_{eff}, i.e. the width of the third eigenstate vanishes at $\varepsilon_w = \varepsilon_b$.

In conclusion, we present numerically computed transmittance through a planar metallic double resonator connected by planar two-dimensional waveguide in figure 41. The total view of the double resonator connected to the semi-infinite waveguide through the diaphragms is shown in figure 39(b). This figure also shows the scattering wave function. Figure 42 presents two patterns of the BICs which correspond to the FP resonances $n = 1$ (a) and $n = 2$ (b) in equation (130).

11. Summary and conclusions

Based on the model two-level (9) or three-level (107) or five-level (132) effective Hamiltonians, we presented an analytical description of how the BICs occur in open systems with further applications for real physical microwave, optical, electron and acoustic systems. Irrespective of the choice of system, the BICs can be classified as SP, Friedrich–Wintgen (FW), FP and accidental. The most obvious case of trapping of resonant modes is related to the symmetry incompatibility of the eigenmodes of the resonator with the propagating mode, i.e. the continuum of the waveguide attached to the resonator. That provides zero coupling of the eigenmode with the continuum. In other words, the SP BICs can be defined as dark modes in view that a probing wave propagating in the continuum cannot 'see' it. Accidental BICs are close to the SP BICs in the meaning that the coupling can vanish, owing to the variation

of parameters of the resonator. We demonstrated these BICs on an example of the Sinai resonator when the motion of the hole inside the symmetric resonator deforms the eigenmodes to result in a zero overlapping integral (see figure 16). It is worth noting that the accidental BICs occur in photonic systems in the form of one- or two-dimensional infinite arrays of dielectric resonators [32, 153], owing to the variation of shape in the resonators or wave vector of the BIC. Also the FP mechanism of BICs is fully transparent, in which a wave is trapped between two mirrors. Off-channel defects [40], volume resonators [16] and one- or two-dimensional periodic structures [46] provide transmission zeros, i.e. mirrors. However the present review addressed first of all the most interesting FW mechanism of localization of waves in the open microwave, optical and acoustic cavities. The mechanism is based on the fullly destructive interference of two resonant modes outgoing from the cavity. Irrespective of the type of the BIC, the complex eigenvalue of the non-Hermitian effective Hamiltonian shows that the BIC point imaginary part of the eigenvalue turns to zero. This phenomenon is a result of the BIC decoupling from the continuum [67].

However, we presented three-dimensional symmetrical cavities, cylindrical and spherical, in which BICs are the result of destructive interference of more resonances. The cavities are opened by attachment of directional waveguides which provide well-separated continua of propagating modes. Therefore, such waveguide systems have the advantage of controlling the number of continua by crossing the cutoff frequencies. Throughout the review we used two almost entirely identical waveguides to obtain identical continua of waveguides. Importantly, the open resonators are one of the best systems where the effective non-Hermitian Hamiltonian can be derived analytically with exact expressions for the coupling matrix. Moreover, the identical waveguides can be attached to the resonant cavities of cylindrical or spherical shapes in such a way that the coupling matrices for the two waveguides differ by phase. This simple way to distinguish the continua gives us an additional parameter to control the wave transmission (wave faucet) and realize twisted BICs.

The evanescent modes with cutoffs above the BIC frequencies also have principal importance for the BICs: first due to the boundary conditions between localized BIC mode and evanescent modes, the BICs exist and slightly stand out from the cavity. Because of the absence of evanescent modes in one-dimensional wires, there are no BICs in the cavity opened by the attachment of half-infinite wires. This is only true for the one-dimensional quantum wires or layered structures where TE and TM polarizations are separated. For the case of spinor fields transmission like one-dimensional electron transmission, through the quantum dot we show that the FW BICs can occur due to the fully destructive interference of resonances with opposite spins. The same idea can be applied to the defect anisotropic layer where EM waves with TE and TM polarization can destructively interfere [136].

Second, the evanescent modes contribute to the Hamiltonian of the closed cavity similarly to the Lamb shift in atomic physics. The coupling to evanescent modes shifts the BIC point from the point of degeneracy of the closed cavity. However, the most striking effect is that the FW BICs exist only owing to the evanescent modes as it was demonstrated in the open spherical cavity.

There are no BICs in the one-dimensional system except specially chosen long-range oscillating potentials by von Neumann and Wigner [1]. However that is true only for scalar waves. For vectorial waves, again the FW mechanism of BICs can be applied, however as a result of fully destructive interference of resonances corresponding to different components of the vectorial field [136].

The spherical resonator demonstrates the unique case of BICs which occur due to coupling of the resonator with directional waveguides as shown in figure 36. The coupling provides the avoided crossing of resonances with different orbital momenta for the variation of the angular position of the one waveguide relative to the other. Previously, the avoided crossing of resonances is achieved owing to the variation of the parameters of the resonator, rectangular cylindrical etc. It is worth noting that the process of the avoided crossing of resonances with the variation of the aspect ratio of isolated dielectric disk gives rise to the resonant modes with extremely high Q factor [154], which is close to the BIC although the bound state in the radiation continuum cannot exist in single dielectric cavity in air [58].

One of the most noteworthy results for the BICs is their existence in photonic crystal systems embedded into the radiation continuum, which has an infinite number of continua because of the dispersion equation $\omega = ck$. It may seem that it is not possible for BICs to be embedded into the radiation continuum. Indeed, rigorous theorem forbids BICs in finite dielectric structures [58]. However, if we take the infinite periodic PhC structures like a 2D PhC surface or a one-dimensional array of dielectric particles, we obtain an analogue of diffraction lattices which are coupled with only discretized continua defined as the diffraction orders. That is a physical explanation for BICs in such infinite PhC structures [31, 60].

Here we skipped the majority of the results on BICs in photonics for two reasons. First, this research direction is developing so rapidly and is so broad that it can hardly be put into a single review. We only included one example of BICs in a one-dimensional photonic crystal holding the defect anisotropic layer in which the BICs are realized because of the fully destructive interference of the resonance with TE and TM polarizations. The second reason is that recent reviews have filled this gap [62–66].

Acknowledgments

First of all, I am grateful to Ingrid Rotter, who introduced me to concept and machinery of non-Hermitian Hamiltonian and with whom we first revealed the phenomenon of the vanishing of resonant width. I would like express gratitude to my colleagues with whom I have worked a long time in the field of bound states in the continuum, Evgeny N Bulgakov, Dmitrii N Maksimov, Konstantin N Pichugin, Artem A Pilipchuk, and Alina Pilipchuk. I also had many discussions with researchers from over all the world: Andrey A Bogdanov, Yi Xu, Dezhuan Han, Egor Muliarov, Ivan Timofeev, Pavel Pankin, Evgeny

Kamenetskii, Andrey Miroshnichenko, Yurii Kivshar, Kirill Koshelev, Ya Yan Lu, and Evgeny Sherman. My special thanks to Monti Segev who encouraged me to write this review.

The work was partially supported by Russian Foundation for Basic Research Projects No. 19-02-00055.

Data availability statement

No new data were created or analysed in this study.

ORCID iDs

Almas F Sadreev https://orcid.org/0000-0002-8690-0100

References

[1] von Neumann J and Wigner E P 1929 Über merkwürdige diskrete eigenwerte *Z. Phys.* **30** 465–7
[2] Stillinger F H and Herrick D R 1975 Bound states in the continuum *Phys. Rev.* A **11** 446–54
[3] Nöckel J U 1992 Resonances in quantum-dot transport *Phys. Rev.* B **46** 15348–56
[4] Weber T A and Pursey D L 1994 Continuum bound states *Phys. Rev.* A **50** 4478–87
[5] Pursey D L and Weber T A 1995 Scattering from a shifted von Neumann–Wigner potential *Phys. Rev.* A **52** 3932–9
[6] Cederbaum L S, Friedman R S, Ryaboy V M and Moiseyev N 2003 Conical intersections and bound molecular states embedded in the continuum *Phys. Rev. Lett.* **90** 013001
[7] Friedrich H and Wintgen D 1985 Interfering resonances and bound states in the continuum *Phys. Rev.* A **32** 3231–42
[8] Feshbach H 1958 Unified theory of nuclear reactions *Ann. Phys., NY* **5** 357–90
[9] Feshbach H 1962 A unified theory of nuclear reactions: II *Ann. Phys., NY* **19** 287–313
[10] Shahbazyan T V and Raikh M E 1994 Two-channel resonant tunneling *Phys. Rev.* B **49** 17123–9
[11] Magunov A I, Rotter I and Strakhova S I 1999 Laser-induced resonance trapping in atoms *J. Phys. B: At. Mol. Opt. Phys.* **32** 1669–84
[12] Volya A and Zelevinsky V 2003 Non-Hermitian effective Hamiltonian and continuum shell model *Phys. Rev.* C **67** 054322
[13] de Guevara M L L, Claro F and Orellana P A 2003 Ghost Fano resonance in a double quantum dot molecule attached to leads *Phys. Rev.* B **67** 195335
[14] Wunsch B and Chudnovskiy A 2003 Quasistates and their relation to the dicke effect in a mesoscopic ring coupled to a reservoir *Phys. Rev.* B **68** 245317
[15] Fedorov M V and Poluektov N P 2004 Two-color interference stabilization of atoms *Phys. Rev.* A **69** 033404
[16] Rotter I and Sadreev A F 2005 Zeros in single-channel transmission through double quantum dots *Phys. Rev.* E **71** 046204
[17] Sadreev A F, Bulgakov E W N and Rotter I 2006 Bound states in the continuum in open quantum billiards with a variable shape *Phys. Rev.* B **73** 235342
[18] de Guevara M L L and Orellana P A 2006 Electronic transport through a parallel-coupled triple quantum dot molecule: Fano resonances and bound states in the continuum *Phys. Rev.* B **73** 205303
[19] Solís B, Ladrón de Guevara M L and Orellana P A 2008 Friedel phase discontinuity and bound states in the continuum in quantum dot systems *Phys. Lett.* A **372** 4736–9
[20] Jin J-M 2010 *Theory and Computation of Electromagnetic Fields* (New York: Wiley)
[21] Lepetit T and Kanté B 2014 Controlling multipolar radiation with symmetries for electromagnetic bound states in the continuum *Phys. Rev.* B **90** 241103(R)
[22] Olendski O and Mikhailovska L 2002 Bound-state evolution in curved waveguides and quantum wires *Phys. Rev.* B **66** 035331
[23] Cattapan G and Lotti P 2007 *S*-matrix poles close to thresholds in confined geometries *Eur. Phys. J.* B **60** 181–5
[24] Cattapan G and Lotti P 2007 Fano resonances in stubbed quantum waveguides with impurities *Eur. Phys. J.* B **60** 51–60
[25] Bolsterli M 1969 Continuity of phase shift at continuum bound state *Phys. Rev.* **182** 1095–6
[26] Robnik M 1986 A simple separable Hamiltonian having bound states in the continuum *J. Phys. A: Math. Gen.* **19** 3845–8
[27] Schult R L, Ravenhall D G and Wyld H W 1989 Quantum bound states in a classically unbound system of crossed wires *Phys. Rev.* B **39** 5476–9
[28] Moiseyev N 2009 Suppression of feshbach resonance widths in two-dimensional waveguides and quantum dots: a lower bound for the number of bound states in the continuum *Phys. Rev. Lett.* **102** 167404
[29] Pilipchuk A S and Sadreev A F 2017 Accidental bound states in the continuum in an open Sinai billiard *Phys. Lett.* A **381** 720–4
[30] Friedrich H and Wintgen D 1985 Physical realization of bound states in the continuum *Phys. Rev.* A **31** 3964–6
[31] Hsu C W, Zhen B, Lee J, Chua S-L, Johnson S G, Joannopoulos J D and Soljačić M 2013 Observation of trapped light within the radiation continuum *Nature* **499** 188–91
[32] Bulgakov E N and Sadreev A F 2014 Bloch bound states in the radiation continuum in a periodic array of dielectric rods *Phys. Rev.* A **90** 053801
[33] Stratton J A 1941 *Electromagnetic Theory* (New York: McGraw-Hill)
[34] Kim C S, Satanin A M, Joe Y S and Cosby R M 1999 Resonant tunneling in a quantum waveguide: effect of a finite-size attractive impurity *Phys. Rev.* B **60** 10962
[35] Sambe H 1973 Steady states and quasienergies of a quantum-mechanical system in an oscillating field *Phys. Rev.* A **7** 2203–13
[36] Sadreev A F 2012 Feshbach projection formalism for transmission through a time-periodic potential *Phys. Rev.* E **86** 056211
[37] Longhi S and Della Valle G 2011 Dynamic reflectionless defects in tight-binding lattices *Phys. Rev.* B **84** 193105
[38] Longhi S and Della Valle G 2013 Floquet bound states in the continuum *Sci. Rep.* **3** 2219
[39] Della Valle G and Longhi S 2014 Floquet–Hubbard bound states in the continuum *Phys. Rev.* B **89** 115118
[40] Fan S, Villeneuve P R, Joannopoulos J D, Khan M J, Manolatou C and Haus H A 1999 Theoretical analysis of channel drop tunneling processes *Phys. Rev.* B **59** 15882–92
[41] Suh W, Wang Z and Fan S 2004 Temporal coupled-mode theory and the presence of non-orthogonal modes in lossless multimode cavities *IEEE J. Quant. Electron.* **40** 1511–8
[42] Rotter I and Sadreev A F 2004 Influence of branch points in the complex plane on the transmission through double quantum dots *Phys. Rev.* E **69** 066201
[43] Sadreev A F, Bulgakov E N and Rotter I 2005 Trapping of an electron in the transmission through two quantum dots coupled by wire *JETP Lett.* **82** 556–61

[44] Sadreev A F, Bulgakov E N and Rotter I 2005 *S*-matrix formalism of transmission through two quantum billiards coupled by a waveguide *J. Phys. A: Math. Gen.* **38** 10647–61

[45] Ordonez G, Na K and Kim S 2006 Bound states in the continuum in quantum-dot pairs *Phys. Rev.* A **73** 022113

[46] Marinica D C, Borisov A G and Shabanov S V 2008 Bound states in the continuum in photonics *Phys. Rev. Lett.* **100** 183902

[47] Bulgakov E N and Sadreev A F 2008 Bound states in the continuum in photonic waveguides inspired by defects *Phys. Rev.* B **78** 075105

[48] Ndangali R F and Shabanov S V 2010 Electromagnetic bound states in the radiation continuum for periodic double arrays of subwavelength dielectric cylinders *J. Math. Phys.* **51** 102901

[49] Sheng Li L and Yin H 2016 Bound states in the continuum in double layer structures *Sci. Rep.* **6** 26988

[50] Sadreev A F, Maksimov D N and Pilipchuk A S 2015 Gate controlled resonant widths in double-bend waveguides: bound states in the continuum *J. Phys.: Condens. Matter* **27** 295303

[51] Hein S and Koch W 2008 Acoustic resonances and trapped modes in pipes and tunnels *J. Fluid Mech.* **605** 401–28

[52] Hein S, Koch W and Nannen L 2012 Trapped modes and Fano resonances in two-dimensional acoustical duct-cavity systems *J. Fluid Mech.* **692** 257–87

[53] Vargiamidis V, Fessatidis V and Horing N J M 2009 Electric-field effects on Fano resonances and transmission phase through quantum wires *J. Appl. Phys.* **106** 043710

[54] Rowe K D and Siemens P J 2005 Unusual quantum effects in scattering wavefunctions of two-dimensional cage potentials *J. Phys. A: Math. Gen.* **38** 9821–47

[55] Bulgakov E and Sadreev A 2011 Formation of bound states in the continuum for a quantum dot with variable width *Phys. Rev.* B **83** 235321

[56] Monticone F and Alù A 2014 Embedded photonic eigenvalues in 3D nanostructures *Phys. Rev. Lett.* **112** 213903

[57] Silveirinha M G 2014 Trapping light in open plasmonic nanostructures *Phys. Rev.* A **89** 023813

[58] Colton D and Kress R 1998 *Inverse Acoustic and Electromagnetic Scattering Theory* 2nd edn (Berlin: Springer)

[59] Yang Y, Peng C, Liang Y, Li Z and Noda S 2014 Analytical perspective for bound states in the continuum in photonic crystal slabs *Phys. Rev. Lett.* **113** 037401

[60] Bulgakov E N and Sadreev A F 2015 Light trapping above the light cone in a one-dimensional array of dielectric spheres *Phys. Rev.* A **92** 023816

[61] Bulgakov E N and Sadreev A F 2017 Bound states in the continuum with high orbital angular momentum in a dielectric rod with periodically modulated permittivity *Phys. Rev.* A **96** 013841

[62] Hsu C W, Zhen B, Stone A D, Joannopoulos J D and Soljačić M 2016 Bound states in the continuum *Nat. Rev. Mater.* **1** 16048

[63] Krasnok A, Baranov D, Li H, Miri M-A, Monticone F and Alú A 2019 Anomalies in light scattering *Adv. Opt. Photon.* **11** 892–951

[64] Koshelev K, Favraud G, Bogdanov A, Kivshar Y and Fratalocchi A 2019 Nonradiating photonics with resonant dielectric nanostructures *Nanophotonics* **8** 725–45

[65] Peng Y and Liao S 2020 Bound states in continuum and zero-index metamaterials: a review (arXiv:2007.01361v1)

[66] Cuesta F S, Asadchy V S, Sayanskiy A D, Lenets V A, Mirmoosa M S, Ma X, Glybovski S B and Tretyakov S A 2020 Nonscattering metasurface-bound cavities for field localization, enhancement, and suppression *IEEE Trans. Antennas Propag.* **68** 1689–703

[67] Bulgakov E N, Rotter I and Sadreev A F 2007 Comment on 'Bound-state eigenenergy outside and inside the continuum for unstable multilevel systems' *Phys. Rev.* A **75** 067401

[68] Kodigala A, Lepetit T, Gu Q, Bahari B, Fainman Y and Kanté B 2017 Lasing action from photonic bound states in continuum *Nature* **541** 196–9

[69] Huang C *et al* 2020 Ultrafast control of vortex microlasers *Science* **367** 1018–21

[70] Wu Y, Kang L, Bao H and Werner D H 2020 Exploiting topological properties of mie-resonance-based hybrid metasurfaces for ultrafast switching of light polarization *ACS Photon.* **7** 2362–73

[71] Jeong K Y, Hwang M S, Kim J, Park J S, Lee J M and Park H G 2020 Recent progress in nanolaser technology *Adv. Mater.* **32** 2001996

[72] Azzam S I, Chaudhuri K, Lagutchev A, Jacob Z, Kim Y L, Shalaev V M, Boltasseva A and Kildishev A V 2020 Single and multi-mode directional lasing from arrays of dielectric nanoresonators (arXiv:2006.16473v1)

[73] Koju V and Robertson W M 2017 Leaky Bloch-like surface waves in the radiation-continuum for sensitivity enhanced biosensors via azimuthal interrogation *Sci. Rep.* **7** 3233

[74] Liu Y, Zhou W and Sun Y 2017 Optical refractive index sensing based on high-q bound states in the continuum in free-space coupled photonic crystal slabs *Sensors* **17** 1861

[75] Romano S, Zito G, Torino S, Calafiore G, Penzo E, Coppola G, Cabrini S, Rendina I and Mocella V 2018 Label-free sensing of ultralow-weight molecules with all-dielectric metasurfaces supporting bound states in the continuum *Photon. Res.* **6** 726

[76] Krasnok A, Caldarola M, Bonod N and Alú A 2018 Spectroscopy and biosensing with optically resonant dielectric nanostructures *Adv. Opt. Mater.* **6** 1701094

[77] Yesilkoy F, Arvelo E R, Jahani Y, Liu M, Tittl A, Cevher V, Kivshar Y and Altug H 2019 Ultrasensitive hyperspectral imaging and biodetection enabled by dielectric metasurfaces *Nat. Photon.* **13** 390–6

[78] Meudt M, Bogiadzi C, Wrobel K and Gorrn P 2019 Hybrid bound states in continuum for enhanced sensing and light manipulation (arXiv:1912.05858v1)

[79] Romano S, Zito G, Managò S, Calafiore G, Penzo E, Cabrini S, De Luca A C and Mocella V 2018 Surface-enhanced Raman and fluorescence spectroscopy with an all-dielectric metasurface *J. Phys. Chem.* C **122** 19738–45

[80] Maksimov D N, Gerasimov V S, Romano S and Polyutov S P 2020 Refractive index sensing with optical bound states in the continuum *Opt. Express* **28** 38907

[81] Ndao A, Hsu L, Cai W, Ha J, Park J, Contractor R, Lo Y and Kanté B 2020 Differentiating and quantifying exosome secretion from a single cell using quasi-bound states in the continuum *Nanophotonics* **9** 1081–6

[82] Chen G Y, Zhang W X and Zhang X D 2019 Strong terahertz magneto-optical phenomena based on quasi-bound states in the continuum and Fano resonances *Opt. Express* **27** 16449

[83] Gorkunov M V, Antonov A A and Kivshar Y S 2020 Metasurfaces with maximum chirality empowered by bound states in the continuum *Phys. Rev. Lett.* **125** 093903

[84] Goos F and Hanchen H 1947 Ein neuer und fundamentaler versuch zur totalreflexion *Ann. Phys., Lpz.* **436** 333–46

[85] Wu F, Wu J, Guo Z, Jiang H, Sun Y, Li Y, Ren J and Chen H 2019 Giant enhancement of the Goos–Hanchen shift assisted by quasibound states in the continuum *Phys. Rev. Appl.* **12** 014028

[86] Jiang X, Tang J, Li Z, Liao Y, Jiang L, Dai X and Xiang Y 2018 Enhancement of photonic spin Hall effect via bound states in the continuum *J. Phys. D: Appl. Phys.* **52** 045401

[87] Rutckaia V, Heyroth F, Schmidt G, Novikov A, Shaleev M, Savelev R, Schilling J and Petrov M 2020 Luminescence enhancement in one-dimensional mie-resonant arrays (arXiv:2006.13185v1)

[88] Ndangali F R and Shabanov S V 2011 The resonant nonlinear scattering theory with bound states in the radiation continuum and the second harmonic generation (arXiv:1107.0468v2)

[89] Krasikov S D, Bogdanov A A and Iorsh I V 2018 Nonlinear bound states in the continuum of a one-dimensional photonic crystal slab *Phys. Rev.* B **97** 224309

[90] Carletti L, Koshelev K, De Angelis C and Kivshar Y 2018 Giant nonlinear response at the nanoscale driven by bound states in the continuum *Phys. Rev. Lett.* **121** 033903

[91] Bulgakov E N and Maksimov D N 2019 Nonlinear response from optical bound states in the continuum *Sci. Rep.* **9** 7153

[92] Anthur A P, Zhang H, Paniagua-Dominguez R, Kalashnikov D A, Ha S T, Maß T W W, Kuznetsov A I and Krivitsky L 2020 Continuous wave second harmonic generation enabled by quasi-bound-states in the continuum on gallium phosphide metasurfaces *Nano Lett.* **20** 8745–51

[93] Pichugin K N and Sadreev A F 2015 Frequency comb generation by symmetry-protected bound state in the continuum *J. Opt. Soc. Am.* B **32** 1630

[94] Wang T and Zhang X 2017 Improved third-order nonlinear effect in graphene based on bound states in the continuum *Photon. Res.* **5** 629

[95] Wang T and Zhang S 2018 Large enhancement of second harmonic generation from transition-metal dichalcogenide monolayer on grating near bound states in the continuum *Opt. Express* **26** 322

[96] Liu Z, Xu Y, Lin Y, Jin X, Feng T, Cao Q, Li J, Lan S and Liu J 2019 High-q quasibound states in the continuum for nonlinear metasurfaces *Phys. Rev. Lett.* **123** 253901

[97] Minkov M, Gerace D and Fan. S 2019 Doubly resonant $\chi(2)$ nonlinear photonic crystal cavity based on a bound state in the continuum *Optica* **6** 1039

[98] Volkovskaya I, Xu L, Huang L, Smirnov A I, Miroshnichenko A E and Smirnova D 2020 Multipolar second-harmonic generation from high-q quasi-BIC states in subwavelength resonators *Nanophotonics* **9** 3953–63

[99] Yuan L and Lu Y Y 2020 Excitation of bound states in the continuum via second harmonic generations *SIAM J. Appl. Math.* **80** 864–80

[100] Ning T, Li X, Zhao Y, Yin L, Huo Y, Zhao L and Yue Q 2020 Giant enhancement of harmonic generation in all-dielectric resonant waveguide gratings of quasi-bound states in the continuum *Opt. Express* **28** 34024

[101] Yang Q, Liu Y, Gan X, Fang C, Han G and Hao Y 2020 Nonlinear bound states in the continuum of etchless lithium niobate metasurfaces *IEEE Photonics J.* **12** 1–9

[102] Raghunathan V, Deka J, Menon S, Biswas R and Lal Krishna A S 2020 Nonlinear optics in dielectric guided-mode resonant structures and resonant metasurfaces *Micromachines* **11** 449

[103] Xiong X, Wu L, Bai P, Png C E, Ong J R and Krivitsky L 2021 Frequency conversion in nano-waveguides using bound-state-in-continuum *Opt. Lett.* **46** 242

[104] Bulgakov E N, Pichugin K N and Sadreev A F 2015 All-optical light storage in bound states in the continuum and release by demand *Opt. Express* **23** 22520

[105] Bulgakov E N and Sadreev A F 2013 Light-induced degeneracy of resonance modes in a nonlinear microcavity coupled with waveguides: application to channel drop filter *J. Opt. Soc. Am.* B **30** 2549

[106] Yu Z, Xi X, Ma J, Tsang H K, Zou C-L and Sun X 2019 Photonic integrated circuits with bound states in the continuum *Optica* **6** 1342

[107] Rotter I 1991 A continuum shell model for the open quantum mechanical nuclear system *Rep. Prog. Phys.* **54** 635–82

[108] Dittes F 2000 The decay of quantum systems with a small number of open channels *Phys. Rep.* **339** 215–316

[109] Okołowicz J, Płoszajczak M and Rotter I 2003 Dynamics of quantum systems embedded in a continuum *Phys. Rep.* **374** 271–383

[110] Savin D V, Sokolov V V and Sommers H-J 2003 Is the concept of the non-Hermitian effective Hamiltonian relevant in the case of potential scattering? *Phys. Rev.* E **67** 026215

[111] Sadreev A F and Rotter I 2003 *S*-matrix theory for transmission through billiards in tight-binding approach *J. Phys. A: Math. Gen.* **36** 11413–33

[112] Maksimov D N, Sadreev A F, Lyapina A A and Pilipchuk A S 2015 Coupled mode theory for acoustic resonators *Wave Motion* **56** 52–66

[113] Pichugin K, Schanz H and Šeba P 2001 Effective coupling for open billiards *Phys. Rev.* E **64** 056227

[114] Mahaux C and Weidenmueller H A 1969 *Shell-Model Approach to Nuclear Reactions* (Amsterdam: North-Holland)

[115] Stöckmann H-J 1999 *Quantum Chaos: An Introduction* (Cambridge: Cambridge University Press)

[116] Alhassid Y 2000 The statistical theory of quantum dots *Rev. Mod. Phys.* **72** 895

[117] Stöckmann H-J, Persson E, Kim Y-H, Barth M, Kuhl U and Rotter I 2002 Effective Hamiltonian for a microwave billiard with attached waveguide *Phys. Rev.* E **65** 066211

[118] Akguc G and Seligman T 2006 Efficient method for scattering problems in open billiards: theory and applications *Phys. Rev.* B **74** 245317

[119] Auerbach N and Zelevinsky V 2011 Super-radiant dynamics, doorways and resonances in nuclei and other open mesoscopic systems *Rep. Prog. Phys.* **74** 106301

[120] Datta S 1995 *Electronic Transport in Mesoscopic Systems* (Cambridge: Cambridge University Press)

[121] Hatano N 2012 Equivalence of the effective Hamiltonian approach and the siegert boundary condition for resonant states *Fortschr. Phys.* **61** 238–49

[122] Hatano N and Ordonez G 2014 Time-reversal symmetric resolution of unity without background integrals in open quantum systems *J. Math. Phys.* **55** 122106

[123] Bulgakov E and Sadreev A 2011 Symmetry breaking in a t-shaped photonic waveguide coupled with two identical nonlinear cavities *Phys. Rev.* B **84** 155304

[124] Fano U 1961 Effects of configuration interaction on intensities and phase shifts *Phys. Rev.* **124** 1866–78

[125] Lyapina A A, Maksimov D N, Pilipchuk A S and Sadreev A F 2015 Bound states in the continuum in open acoustic resonators *J. Fluid Mech.* **780** 370–87

[126] Moiseyev N 1998 Quantum theory of resonances: calculating energies, widths and cross-sections by complex scaling *Phys. Rep.* **302** 212–93

[127] Kikkawa R, Nishida M and Kadoya Y 2019 Polarization-based branch selection of bound states in the continuum in dielectric waveguide modes anti-crossed by a metal grating *New J. Phys.* **21** 113020

[128] Markoš P and Soukoulis C M 2008 *Wave Propagation: From Electrons to Photonic Crystals and Left-Handed Materials* (Princeton, NJ: Princeton University Press)

[129] Anderson P W 1958 Absence of diffusion in certain random lattices *Phys. Rev.* **109** 1492–505

[130] Aharonov Y and Bohm D 1959 Significance of electromagnetic potentials in the quantum theory *Phys. Rev.* **115** 485–91

[131] Bulgakov E N, Pichugin K N, Sadreev A F and Rotter I 2006 Bound states in the continuum in open Aharonov–Bohm rings *JETP Lett.* **84** 430–5

[132] Xia J-B 1992 Quantum waveguide theory for mesoscopic structures *Phys. Rev.* B **45** 3593–9

[133] Smirnov V I 1964 *A Course of Higher Mathematics* vol 3 (Oxford: Pergamon)
[134] Texier C 2002 Scattering theory on graphs: II. The friedel sum rule *J. Phys. A: Math. Gen.* **35** 3389–407
[135] Texier C and Buttiker M 2003 Local friedel sum rule on graphs *Phys. Rev.* B **67** 245410
[136] Pankin P S, Wu B-R, Yang J-H, Chen K-P, Timofeev I V and Sadreev A F 2020 One-dimensional photonic bound states in the continuum *Commun. Phys.* **3** 91
[137] Jackson J D 1962 *Classical Electrodynamics* (New York: Wiley)
[138] Bonnet-Bendhia A-S and Starling F 1994 Guided waves by electromagnetic gratings and non-uniqueness examples for the diffraction problem *Math. Methods Appl. Sci.* **17** 305–38
[139] Rotter S, Libisch F, Burgdorfer J, Kuhl U and Stockmann H-J 2004 Tunable Fano resonances in transport through microwave billiards *Phys. Rev.* E **69** 046208
[140] Lyapina A A, Pilipchuk A S and Sadreev A F 2018 Bound states with orbital angular momentum in the continuum of cylindrical non-axisymmetric waveguide *Ann. Phys., NY* **396** 56–70
[141] Lyapina A A, Pilipchuk A S and Sadreev A F 2018 Trapped modes in a non-axisymmetric cylindrical waveguide *J. Sound Vib.* **421** 48–60
[142] Remacle F, Munster M, Pavlov-Verevkin V B and Desouter-Lecomte M 1990 Trapping in competitive decay of degenerate states *Phys. Lett.* A **145** 265–8
[143] Zhen B, Hsu C W, Lu L, Stone A D and Soljačić M 2014 Strong resonances on periodic arrays of cylinders and optical bistability with weak incident waves *Phys. Rev. Lett* **113** 257401
[144] Bulgakov E N and Sadreev A F 2016 Spin polarized bound states in the continuum in open Aharonov–Bohm rings with the Rashba spin–orbit interaction *J. Phys.: Condens. Matter* **28** 265301
[145] Dai S, Liu L, Han D and Zi J 2018 From topologically protected coherent perfect reflection to bound states in the continuum *Phys. Rev.* B **98** 081405
[146] Sadreev A F, Pilipchuk A S and Lyapina A A 2017 Tuning of Fano resonances by rotation of continuum: wave faucet *Europhys. Lett.* **117** 50011
[147] Sadreev A F, Pilipchuk A S and Pilipchuk A A 2018 Tuning of Fano resonance by waveguide rotation *Fano Resonances in Optics and Microwaves* (*Springer Series in Optical Sciences*) (Switzerland: Springer) p 497
[148] Born M and Wolf E 1999 *Principles of Optics: Electromagnetic Theory of Propagation, Interference and Diffraction of Light* (Cambridge: Cambridge University Press)
[149] Miroshnichenko A E and Kivshar Y S 2005 Engineering fano resonances in discrete arrays *Phys. Rev.* E **72** 056611
[150] Wang Z and Fan S 2003 Compact all-pass filters in photonic crystals as the building block for high-capacity optical delay lines *Phys. Rev.* E **68** 066616
[151] Lin L-L, Li Z-Y and Lin B 2005 Engineering waveguide-cavity resonant side coupling in a dynamically tunable ultracompact photonic crystal filter *Phys. Rev.* B **72** 165330
[152] Lee H-W 1999 Generic transmission zeros and in-phase resonances in time-reversal symmetric single channel transport *Phys. Rev. Lett.* **82** 2358–61
[153] Hsu C W, Zhen B, Chua S-L, Johnson S G, Joannopoulos J D and Soljačić M 2013 Bloch surface eigenstates within the radiation continuum *Light. Sci. Appl.* **2** e84
[154] Rybin M V, Koshelev K L, Sadrieva Z F, Samusev K B, Bogdanov A A, Limonov M F and Kivshar Y S 2017 High-q supercavity modes in subwavelength dielectric resonators *Phys. Rev. Lett.* **119** 243901